

Draft of June 25, 2018

Resolved Inner Disks around Herbig Ae/Be Stars

J.A. Eisner¹, B.F. Lane², L.A. Hillenbrand¹, R.L. Akeson³, & A.I. Sargent¹

jae@astro.caltech.edu

ABSTRACT

We have observed 14 Herbig Ae/Be sources with the long-baseline near-IR Palomar Testbed Interferometer. All except two sources are resolved at 2.2 μm , with angular sizes generally $\lesssim 5$ mas. We determine the size scales and orientations of the 2.2 μm emission using various models: uniform disks, Gaussians, uniform rings, flat accretion disks with inner holes, and flared disks with puffed-up inner rims. Although it is difficult to distinguish different radial distributions, we are able to place firm constraints on the inclinations of most sources; 7 objects display significantly inclined morphologies. The inner disk inclinations derived from our near-IR data are generally compatible with the outer disk geometries inferred from millimeter interferometric observations, implying that HAEBE disks are not significantly warped. Using the derived inner disk sizes and inclinations, we compute the spectral energy distributions for two simple physical disk models, and compare these with observed SEDs compiled from the literature and new near-IR photometry. While geometrically flat accretion disk models are consistent with the data for the earliest spectral types in our sample (MWC 297, V1685 Cyg, and MWC 1080), the later-type sources are explained better through models incorporating puffed-up inner disk walls. The different inner disk geometries may indicate different accretion mechanisms for early and late-type Herbig Ae/Be stars.

Subject headings: stars:pre-main sequence—stars:circumstellar matter—stars:individual(AB Aur,MWC 480,MWC 758, CQ Tau,T Ori,MWC 120,HD 141569,HD 158352,MWC 297,VV Ser,V1295 Aql,V1685 Cyg, AS 442,MWC 1080)—techniques:high angular resolution—techniques:interferometric

¹California Institute of Technology, Department of Astronomy MC 105-24, Pasadena, CA 91125

²Center for Space Research, MIT Department of Physics, 70 Vassar Street, Cambridge, MA 02139

³California Institute of Technology, Michelson Science Center MC 100-22, Pasadena, CA 91125

1. Introduction

Herbig Ae/Be (HAEBE; Herbig 1960) stars are intermediate-mass ($2\text{--}10 M_{\odot}$) young stellar objects that show broad emission lines, rapid variability, and excess infrared and millimeter-wavelength emission. These properties are consistent with the presence of hot and cold circumstellar dust and gas. While there is still some debate about the morphology of this circumstellar material, most evidence supports the hypothesis that in many cases the dust and gas lie in massive ($\sim 0.01 M_{\odot}$) circumstellar disks (Natta et al. 2000; Hillenbrand et al. 1992).

The strongest evidence for circumstellar disks around HAEBE stars comes from near-IR and millimeter interferometry. Flattened structures around several sources have been resolved on $\lesssim 1$ AU scales in the near-IR (Eisner et al. 2003, hereafter, ELAHS) and on ~ 100 AU scales at millimeter wavelengths (Mannings & Sargent 1997; Mannings & Sargent 2000; Piétu et al. 2003), and detailed kinematic modeling of one source, MWC 480, is consistent with rotation in a Keplerian disk (Mannings et al. 1997; Simon et al. 2001). $H\alpha$ spectropolarimetric observations, which trace dust on scales of tens of stellar radii (Vink et al. 2002), and modeling of forbidden emission lines that arise in winds and outflows around HAEBE stars (Corcoran & Ray 1997) provide further evidence for disks. Finally, disk-like distributions of material around HAEBEs are suggested by modeling of spectral energy distributions (SEDs). Various models, including geometrically flat accretion disks (e.g., Hillenbrand et al. 1992), flared outer disks (e.g., Chiang & Goldreich 1997), and puffed-up inner disk rims (Dullemond, Dominik, & Natta 2001; hereafter DDN), have been used to fit the data (although the SEDs for some sources can also be explained by more spherically distributed dust; e.g., Hartmann et al. 1993).

Previous near-IR interferometric observations probed the inner disks around several HAEBE sources (Akeson et al. 2000; Millan-Gabet, Schloerb, & Traub 2001, hereafter MST; ELAHS; Wilkin & Akeson 2003; see also aperture masking results, Danchi, Tuthill, & Monnier 2001; Tuthill et al. 2002). Here, we expand the sample and obtain superior $u - v$ coverage, enabling measurements of size scales and orientations of the inner disks around 14 HAEBEs. We present results for AB Aur, MWC 480, MWC 758, CQ Tau, T Ori, MWC 120, HD 141569, HD 158352, VV Ser, MWC 297, V1295 Aql, V1685 Cyg (BD+40°4124), AS 442, and MWC 1080. Two sources, HD 141569 and HD 158352, show no evidence of near-IR circumstellar emission and appear unresolved in our interferometric observations. The other 12 sources in our sample show resolved circumstellar emission, consistent with disks.

We model the structure of circumstellar dust within $\sim 0.1\text{--}1$ AU of these HAEBE stars, fitting three simple geometrical models (Gaussians, uniform disks, and uniform rings), and two basic physical models (flat accretion disks with inner holes and flared passive disks with

puffed-up inner walls). For each model, we determine approximate size scales, position angles, and inclinations of the near-IR circumstellar emission. Where possible, we compare our 2.2 μm interferometry results with previously published 1.6 μm and 2.2 μm interferometric data from the IOTA interferometer (MST). In addition, we compare our results with SEDs compiled from the literature and new data, and millimeter interferometric results (where available), in order to further constrain simple physical models of HAEBE disks.

2. Observations and Calibration

The Palomar Testbed Interferometer (PTI) is a fringe-tracking long-baseline near-IR Michelson interferometer located on Palomar Mountain near San Diego, CA (Colavita et al. 1999). PTI combines starlight from two 40-cm aperture telescopes using a Michelson beam combiner, and the resulting fringe visibilities provide a measure of the brightness distribution on the sky (via the van Cittert-Zernike theorem). PTI measures normalized squared visibilities, V^2 , which provide unbiased estimates of the visibility amplitudes (Colavita 1999); V^2 is unity for point sources and smaller for resolved sources.

We observed 14 HAEBE sources with PTI between May, 2002 and January, 2004. Properties of the sample are included in Table 1. We obtained K-band ($\lambda_0 = 2.2 \mu\text{m}$, $\Delta\lambda = 0.4 \mu\text{m}$) measurements on an 85-m North-West (NW) baseline for all 14 objects, on an 86-m South-West (SW) baseline for 8, and on a 110-m North-South (NS) baseline for 6. The NW baseline is oriented 109° west of north and has a fringe spacing of ~ 5 mas, the SW baseline is 211° west of north with a ~ 5 mas fringe spacing, and the NS baseline is 160° west of north and has a fringe spacing of ~ 4 mas. A summary of the observations is given in Table 2.

For the sample, V^2 were measured from a synthetic wide-band channel formed from five spatially-filtered spectral pixels covering the K-band (Colavita 1999). Since PTI tracks the central (“white light”) fringe, and the fringe spacings for PTI baselines are much smaller than the interferometric field of view (~ 50 mas; set by baseline lengths and spectral bandpass), the effects of spectral smearing on the K-band visibilities are negligible.

The visibilities were calibrated by observing sources of known angular size. Our adopted angular size for a calibrator is the average of three estimates based on 1) published stellar luminosity and distance, 2) a blackbody fit to published photometric data with the temperature constrained to that expected for the published spectral type, and 3) an unconstrained blackbody fit to the photometric data. We propagate the errors on individual estimates to determine the uncertainty of the average size. Relevant properties of the calibrators used

in these observations are given in Table 3. For a more thorough discussion of the data measurement and calibration procedures, see ELAHS.

2.1. PALAO Observations

In addition to the PTI data, we obtained adaptive optics images of the sources in our sample. As we discuss in §3.1, the adaptive optics data help distinguish between components of the PTI visibilities, including circumstellar emission, the central stars, and nearby companions.

Using the Palomar 200-inch adaptive optics system (PALAO; Troy et al. 2000) with the PHARO camera (Hayward et al. 2001) on November 17-18, 2002, January 13-14, 2003, and July 14-15, 2003, we imaged our sources in the JHK bands with a 25 mas plate scale and a 25" field of view. We used 1% or 0.1% neutral density filters and short integration times to prevent saturation of the camera. After bias correction, flat-fielding, and background subtraction, the reduced images enabled searches for any companions $\gtrsim 0''.05$ away from the target sources. Source counts were obtained from aperture photometry with sky subtraction, and photometric calibration was achieved using nearby sources with measured 2MASS photometry. The determined JHK magnitudes of our target sources are listed in Table 1. While the single-night uncertainty of the photometry is typically < 0.05 mags, night-to-night variations (due to variable seeing and small instrumental changes) limit the photometric accuracy to ~ 0.15 mags. Since AS 442 appears to be variable with a short timescale (probably days), Table 1 quotes the average of two measurements. For all objects, our photometry is consistent with previously published measurements to within ~ 0.3 magnitudes (2MASS; Hillenbrand et al. 1992; Malfait et al. 1998; de Winter et al. 2001; Eiroa et al. 2001).

3. Modeling

From the PTI data, we measured calibrated squared visibilities for all sources listed in Table 1. For each source, we constrain the angular size and geometry of the emission by fitting the visibility data with several simple models: Gaussians, uniform disks, uniform rings, flat accretion disks with inner holes, and flared passive disks with puffed-up inner walls. In this section, we describe the models, as well as corrections to the visibilities required to separate the circumstellar component from contributions by the central stars or nearby companions.

3.1. Visibility Corrections

3.1.1. Nearby Companions

Nearby companions that lie outside the interferometric field of view, ~ 50 mas, but within the field of view of the detector, $\sim 1''$, will contribute incoherent light to the visibilities, leading to measured visibilities smaller than the true values:

$$\frac{V_{\text{true}}^2}{V_{\text{meas}}^2} = \left(\frac{1}{1 + 10^{-\Delta K/2.5}} \right)^2, \quad (1)$$

where ΔK is the difference in K-band magnitudes between the two stars. Our PALAO Adaptive optics images of the sources in our sample (§2.1) show that most of these have no bright companions ($\Delta K < 5$) at distances between ~ 50 mas and $1''$, and thus no companion corrections are required ($V_{\text{true}}^2/V_{\text{meas}}^2 > 0.98$). For MWC 1080, we measured $\Delta K = 2.70$ for a companion at $0''.78$ separation (consistent with previous measurements by Corporon 1998) and Equation 1 yields a correction factor of 0.85. V1685 Cyg is also known to have a faint companion ($\Delta K = 5.50$; Corporon 1998), but its effects on the visibilities are negligible.

3.1.2. Stellar Emission

We account for the effect of the central star on the visibilities by including it in the models:

$$V_{\text{tot}}^2 = \left(\frac{F_* V_* + F_x V_x}{F_* + F_x} \right)^2 \approx \left(\frac{F_* + F_x V_x}{F_* + F_x} \right)^2, \quad (2)$$

where F_* is the stellar flux, F_x is the excess flux (both measured at $2.2 \mu\text{m}$), $V_* \approx 1$ is the visibility of the (unresolved) central star, and V_x is the visibility due to the circumstellar component. It is reasonable to assume that $V_* \approx 1$, since for the stellar radii ($\sim 2\text{--}9 R_\odot$) and distances ($\sim 140\text{--}1000$ pc) for our sample, the angular diameters of the central stars will be < 0.2 mas. In the case of the binary model described below (§3.2.4), we do not perform any such correction, since the basic model already includes the stellar component.

Since HAEBE objects are often variable at near-IR wavelengths (e.g., Skrutskie et al. 1996), we obtained nearly contemporaneous photometric K-band measurements for our sample, as described in §2.1. As in ELAHS, we calculate F_* and F_x using our K-band photometry (Table 1) combined with BVRI photometry, visual extinctions, stellar radii, and effective temperatures from the literature (Herbst & Shevchenko 1999; Hillenbrand et al. 1992; Oudmaijer et al. 2001; de Winter et al. 2001; Eiroa et al. 2002; Vieira et al. 2003; Bigay & Garnier 1970)

For several sources where literature values were not available, we computed the stellar parameters using the published spectral types and photometry. The spectral type gives the effective temperature and expected color, from which we determine the extinction. We determine the stellar luminosity (using the adopted distance from Table 1) from a bolometric correction applied to the optical photometry, and stellar radius is given by the Stephan-Boltzmann equation. Assuming that all of the short-wavelength flux is due to the central star, we fit a blackbody at the assumed effective temperature to the de-reddened BVRI data. De-reddening uses the extinction law of Steenman & Thé (1991). The K-band stellar flux, F_* , is derived from the value of this blackbody curve at $2.2 \mu\text{m}$, and the excess flux, F_x , is given by the difference between the de-reddened observed flux and the stellar flux. The derived fluxes are given in Table 1.

The uncertainties in our K-band photometric measurements (~ 0.15 mags) and the uncertainties in the optical photometry used to determine the stellar contributions to the K-band fluxes lead to some uncertainties in the sizes inferred from the interferometric data. This uncertainty decreases for larger F_x/F_* ratios, and is typically $\lesssim 0.1$ mas for the sources discussed here. CQ Tau, VV Ser, V1685 Cyg, and AS 442 are optically variable by $\Delta V \gtrsim 1$ magnitudes on timescales of days to months (while the other sources in our sample show little or no optical variability; Herbst & Shevchenko 1999), and thus F_* is somewhat uncertain. However, since $F_x/F_* \gg 1$ for these objects, this uncertainty is relatively unimportant when modeling the visibilities.

Uncertainties in the calculation of stellar and circumstellar fluxes can also have a small effect on the measured inclinations. However, since the fluxes for our sample are dominated by the excess component, only large errors ($> 100\%$) in the flux estimation will produce measurable effects on the determined inclinations. Since our photometric errors are generally $\lesssim 10\%$, the effect on measured inclinations is negligible.

3.1.3. *Extended Emission*

Equation 2 assumes that the point-like central star and compact circumstellar emission contribute coherently to the visibilities. There may also be an incoherent component due to extended emission (either thermal or scattered) from tenuous dust. The excess flux, F_x , would then be the sum of the compact circumstellar emission, F_{comp} , and the extended emission, F_{ext} . Including the incoherent contribution in the visibilities would modify Equation 2 to:

$$V_{\text{tot}}^2 = \left(\frac{F_* + F_{\text{comp}} V_{\text{comp}}}{F_* + F_{\text{comp}} + F_{\text{ext}}} \right)^2 = \left(\frac{F_* + [F_x - F_{\text{ext}}] V_x}{F_* + F_x} \right)^2, \quad (3)$$

causing a reduction in the measured visibilities.

The existence of dust on large angular scales around some Herbig Ae/Be stars is illustrated by optical light scattered from dust grains far from the star (e.g., Grady et al. 1999). Furthermore, SED models that include large-scale optically thin dust, in addition to disks, usually fit the data well for HAEBE sources (Vinković et al. 2003, and references therein). Nevertheless, these observations do not measure the exact contribution of extended K-band emission, and our adaptive optics observations (§2.1) do not have sufficient sensitivity to detect faint emission above the halo of the point spread function within $1''$ (the PTI field of view) of the central stars. Thus, we do not include the effect of incoherent emission when modeling the visibilities; i.e., we use Equation 2 in the analysis below.

Because our measured visibilities are found to depend on projected baseline (see §4.1), contrary to the baseline-independent visibilities expected for incoherent emission, the incoherent contribution is probably insignificant compared to the compact circumstellar component. Although small incoherent contributions may lead to estimated size scales slightly larger than true values, we show below in §4.2 that the effect is likely to be quite small, perhaps as high as a few percent in the worst case.

3.2. Compact Circumstellar Emission

For each source, we compare the observed visibilities to those derived from a uniform disk model, a Gaussian model, a ring model, a geometrically flat accretion disk model with an inner hole, and a flared passive disk with a puffed-up inner wall; all models are 2-D. The uniform disk, Gaussian, ring, and flat accretion disk models were discussed in ELAHS, and the basic equations are merely recalled here. In addition, we develop and implement a flared disk model with a puffed-up inner wall, which is a more physically plausible model than any of those considered in ELAHS.

As in ELAHS, we consider both face-on and inclined models. If we assume that the inclination of the circumstellar material is zero, then the one remaining free parameter in the models is the angular size scale, θ . When we include inclination effects, we fit for three parameters: size (θ), inclination angle (ϕ), and position angle (ψ). Inclination is defined such that a face-on disk has $\phi = 0$, and position angle, ψ , is measured east of north. Inclination effects are included in the models via a simple coordinate transformation:

$$x' = x \sin \psi + y \cos \psi; \quad y' = \frac{y \sin \psi - x \cos \psi}{\cos \phi}, \quad (4)$$

$$u' = u \sin \psi + v \cos \psi; \quad v' = \cos \phi(v \sin \psi - u \cos \psi). \quad (5)$$

Here, $(x, y), (u, v)$ are the original sky and $u - v$ plane coordinates, and $(x', y'), (u', v')$ are the transformed coordinates.

In addition to these five models, we also examine whether the data are consistent with a wide binary model, which we approximate as two stationary point sources. For this model, the free parameters are the angular separation (θ), the position angle (ψ), and the brightness ratio of the two components (R).

We fit these models to the PTI data for each source by searching grids of parameters for the minimum χ_r^2 value. The grid for face-on disk models was generated by varying θ from 0.01 to 10 mas in increments of 0.01 mas. For sources with adequate $u - v$ coverage (Figure 1), we also fit inclined disk models, where in addition to varying θ , we vary ϕ from 0° to 90° and ψ from 0° to 180° , both in increments of 1° . Since inclined disk models are symmetric under reflections through the origin, we do not explore position angles between 180° and 360° . For the binary model, we vary θ from 1 to 100 mas in increments of 0.01 mas, ψ from 0° to 180° in increments of 1° , and $R = F_2/F_1$ from 0.2 to 1 in increments of 0.001 (for flux ratios < 0.2 or angular separations < 1 mas, the effects of the companions on the visibilities will be negligible, and we can rule out angular separations $\gtrsim 100$ mas from adaptive optics imaging). Although binary models are not symmetric under reflections through the origin, PTI does not measure phase and cannot distinguish 180° -rotated models; thus, we only consider position angles from 0° to 180° .

For each point in the parameter grid, we generate a model for the observed $u - v$ coverage, and calculate the reduced chi squared, χ_r^2 , to determine the “best-fit” model. Standard $1-\sigma$ confidence limits for face-on models are determined by finding the grid points where the non-reduced χ^2 equals the minimum value plus 1. For inclined disk or binary models, the errors on each parameter correspond to an increment of 3.5 of the the minimum χ^2 surface. The quoted uncertainties are not scaled by χ_r^2 .

3.2.1. Simple Geometrical Disk Models

The normalized visibilities for a Gaussian, uniform disk, and uniform ring brightness distribution are,

$$V_{\text{gauss}}(r_{\text{uv}}) = \exp\left(-\frac{\pi^2 \theta^2 r_{\text{uv}}^2}{4 \ln 2}\right), \quad (6)$$

$$V_{\text{uniform}}(r_{\text{uv}}) = 2 \frac{J_1(\pi \theta r_{\text{uv}})}{\pi \theta r_{\text{uv}}}, \quad (7)$$

$$V_{\text{ring}} = \frac{2}{\pi \theta r_{\text{uv}} (2f + f^2)} [(1 + f) J_1([1 + f] \pi \theta r_{\text{uv}}) - J_1(\pi \theta r_{\text{uv}})]. \quad (8)$$

Here, (x, y) are the angular offsets from the central star, θ is the angular size scale (FWHM, diameter, and inner diameter for the Gaussian, uniform disk, and ring models, respectively), and r_{uv} is the “uv radius”:

$$r_{\text{uv}} = (u^2 + v^2)^{1/2}. \quad (9)$$

For the ring model, $f = W/R$, where R is the radius of the inner edge of the ring, and W is the width of the ring. In order to facilitate comparison of this model to the more physical puffed up inner disk models (§3.2.3), we use ring widths derived from radiative transfer modeling by DDN (Table 1); for stars earlier than spectral type B6, we assume $f = 0.27$, and for stars later than B6, we assume $f = 0.18$. The models for the observed squared visibilities are obtained by substituting Equations 6, 7, or 8 for V_x in Equation 2.

3.2.2. Geometrically Flat Accretion Disk Model

We derive the brightness distribution and predicted visibilities for a geometrically thin irradiated accretion disk by determining the temperature and spectral energy distributions for a series of annuli extending from some inner radius, R_{in} , to some outer radius, R_{out} . We then weight the visibilities for each annulus (which are given by the ring visibilities described by Equation 8) by their SEDs to determine the visibilities expected for the entire disk.

For a disk heated by stellar radiation and accretion (Lynden-Bell & Pringle 1974), the temperature profile, T_{R} , in the regime where $R_*/R \ll 1$, is given by $T_{1\text{AU}} (R/\text{AU})^{-3/4}$. Here, $T_{1\text{AU}} = T_{\text{in}} (R_{\text{in}}/\text{AU})^{3/4}$, where T_{in} is the temperature at the inner radius. We consider two values of T_{in} : 1500 K and 2000 K. These are likely (upper limit) sublimation temperatures for silicate and graphite grains, respectively (e.g., Salpeter 1977; Pollack et al. 1994), and it is reasonable to assume that there is little or no dust emission interior to R_{in} (although the model does not exclude the possibility of optically thin gas interior to R_{in}). We choose R_{out} to be the lesser of 100 AU or the radius at which $T_{\text{R}} = 10$ K (R_{out} is not important in this analysis, since virtually all of the near-IR flux comes from the hotter inner regions of the disk).

The flux in an annulus specified by inner boundary R_i and outer boundary R_f is given by

$$F_{\text{annulus}} = \frac{\pi}{d^2} [B_\nu(T_i) + B_\nu(T_f)] R_i (R_f - R_i) \cos(\phi), \quad (10)$$

and the normalized visibilities for this annulus are (following Equation 8):

$$V_{\text{annulus}} = \frac{2}{\pi r_{\text{uv}} (\theta_f^2 - \theta_i^2)} [\theta_f J_1(\pi \theta_f r_{\text{uv}}) - \theta_i J_1(\pi \theta_i r_{\text{uv}})]. \quad (11)$$

Here, d is the distance to the source, ν is the observed frequency, B_ν is the Planck function, T is the temperature, R is the physical radius, θ is the angular size, ϕ is the inclination, r_{uv} is the “uv radius” (Equation 9), and i, f indicate the inner and outer boundaries of the annulus. To obtain the visibilities for the entire disk, we sum the flux-weighted visibilities for each annulus and normalize by the total flux:

$$V_{\text{disk}} = \frac{\sum_{R_{\text{in}}}^{R_{\text{out}}} F_{\text{annulus}} V_{\text{annulus}}}{\sum_{R_{\text{in}}}^{R_{\text{out}}} F_{\text{annulus}}}. \quad (12)$$

The resultant model visibilities are obtained by substituting this expression for V_x into Equation 2.

As mentioned above, we compute the visibilities for models using $T_{\text{in}} = 1500, 2000$ K. The main effect of T_{in} is that for lower temperatures, the flux difference between the inner several annuli is significantly larger (since we are on the Wien tail of the blackbody curve), leading to a smaller flux-weighted emitting region probed by the $2.2 \mu\text{m}$ visibilities. This smaller effective area for lower T_{in} leads to a slightly larger inner disk diameter (Equation 8). In practice, T_{in} is not a critical parameter since most of the $2.2 \mu\text{m}$ radiation in the disk comes from the innermost annulus.

3.2.3. Puffed-Up Inner Disk Model

We consider a two-layer flared disk model (Chiang & Goldreich 1997) with a puffed-up inner disk wall (DDN). The primary difference between this model and the geometrically flat model discussed above is the angle at which starlight is incident on the disk. While starlight tends to hit a flat disk at grazing angles, for this model the starlight is incident at larger angles and causes more heating of the disk at a given radius. This additional heating causes the disk to expand in the vertical direction (in order to maintain hydrostatic equilibrium), which leads to a puffed-up inner wall as well as flaring in the outer disk. Since stellar radiation is incident on the inner wall normally, most of the $2.2 \mu\text{m}$ flux is generated in this region.

As in the case of a geometrically flat disk (§3.2.2) we first calculate the radial temperature and SED distributions. The temperature distribution for this model has been discussed in detail by Chiang & Goldreich (1997) and DDN, but we present a brief outline of the equations here. For the flared two-layer disk we assume a radial dust surface density profile $\Sigma(R) = 10^5 (R/1\text{AU})^{-1.5} \text{ g cm}^{-2}$ and a flaring angle, α , which defines the angle at which

starlight impacts the disk:

$$\alpha = 0.4 \left(\frac{R_*}{R} \right) + \frac{8}{7} \left(\frac{T_*}{T_c} \right)^{4/7} \left(\frac{R}{R_*} \right)^{2/7}. \quad (13)$$

Here, R is the radial coordinate in the disk, $T_c = GM_*\mu m_p/kR_*$, M_* is the mass of the star, μ is the mean molecular weight, R_* is the stellar radius, and T_* is the stellar temperature. We define a flaring index, ξ , which corresponds to the exponent on the scale height as a function of radius minus one ($\gamma - 1$ in DDN). Following a simple hydrostatic equilibrium calculation from Chiang & Goldreich (1997), we have adopted a value for ξ of $2/7$.

Assuming that the opacity in the disk is due to silicate dust (Draine & Lee 1984), we parameterize the opacity of the surface and interior layers using ψ_{surf} and ψ_{int} :

$$\psi_{\text{surf}} = \frac{\sum_{\nu=0}^{\infty} B_{\nu}(T_{\text{surf}})\kappa_{\nu} (1 - \exp[-\Sigma(R)\kappa_{\nu}])}{\sum_{\nu=0}^{\infty} B_{\nu}(T_{\text{surf}})\kappa_{\nu}}, \quad (14)$$

$$\psi_{\text{int}} = \frac{\sum_{\nu=0}^{\infty} B_{\nu}(T_{\text{int}}) (1 - \exp[-\Sigma(R)\kappa_{\nu}])}{\sum_{\nu=0}^{\infty} B_{\nu}(T_{\text{int}})}. \quad (15)$$

The temperature of the surface layer is determined from

$$T_{\text{surf}} = \epsilon_s^{-0.25} \left(\frac{R_*}{2R} \right)^{0.5} T_*. \quad (16)$$

Here, $\epsilon_s = \kappa_p(T_{\text{surf}})/\kappa_p(T_*)$, where κ_p is the Planck mean opacity. The interior temperature is then given by

$$T_{\text{int}} = \left(\frac{\alpha\psi_{\text{surf}}}{2\psi_{\text{int}}} \right)^{0.25} \left(\frac{R_*}{R} \right)^{0.5} T_*. \quad (17)$$

Equations 14–17 are solved iteratively. The SED of an annulus is given by summing the contributions from the surface and the interior. We denote the surface temperatures at the inner and outer radii of the annulus by $T_{\text{si}}, T_{\text{sf}}$, and the interior temperatures by $T_{\text{ii}}, T_{\text{if}}$. The surface component of the SED is given by

$$F_{\text{surf}} = \frac{\pi}{d^2} [B_{\nu}(T_{\text{si}}) + B_{\nu}(T_{\text{sf}})] R_i (R_f - R_i) (1 + \exp[-\Sigma(R_i)\kappa_{\nu}/\cos(\phi)]) \kappa_{\nu} \Delta\Sigma, \quad (18)$$

where

$$\Delta\Sigma = \frac{\psi_{\text{int}}}{\psi_{\text{surf}}} \left(\frac{T_{\text{ii}}}{T_{\text{si}}} \right)^4 \frac{1}{2\kappa_p}. \quad (19)$$

For the interior,

$$F_{\text{int}} = \frac{\pi}{d^2} [B_{\nu}(T_{\text{ii}}) + B_{\nu}(T_{\text{if}})] R_i (R_f - R_i) (1 - \exp[-\Sigma(R_i)\kappa_{\nu}/\cos(\phi)]) \cos(\phi). \quad (20)$$

In addition to the surface and interior layers of the disk, a puffed-up inner disk wall is included in the model. We choose the radius of this inner rim, R_{in} , to be the radius where $T = T_{\text{in}}$ (R_{in} also defines the inner radius of the flared disk component). We consider $T_{\text{in}} = 1500, 2000$ K, likely sublimation temperatures of graphite and silicate grains, respectively. Because the wall is directly exposed to stellar radiation (instead of the glancing angles encountered in a geometrically thin disk model), the inner rim puffs up, attaining a height given by

$$H_{\text{rim}} = \chi_{\text{rim}} \sqrt{\frac{kT_{\text{in}}R_{\text{in}}^3}{\mu m_{\text{p}}GM_*}}. \quad (21)$$

χ_{rim} is a dimensionless quantity that describes how the disk height depends on the stellar luminosity. For the stars in our sample, we adopt typical values of $\chi_{\text{rim}} = 5.3$ for stars later than spectral type B6, and $\chi_{\text{rim}} = 4.5$ for earlier spectral types (DDN). The emergent flux from the rim contributes only to the innermost annulus:

$$F_{\text{rim}}(R_{\text{in}}) = \frac{4R_{\text{in}}H_{\text{rim}}}{d^2} B_{\nu}(T_{\text{in}}). \quad (22)$$

While DDN included the effects of inclination, for simplicity we ignore those here. In effect, this corresponds to assuming a different shape for the inner disk wall; DDN assumed a thin cylindrical annulus, and we adopt a more toroidal shape.

The total flux for each annulus is given by

$$F_{\text{annulus}} = F_{\text{int}} + F_{\text{surf}} + F_{\text{rim}}, \quad (23)$$

where F_{rim} is zero everywhere but the innermost annulus. To determine the visibilities for the entire disk, we sum the flux-weighted visibilities for each annulus, and normalize by the total flux (Equation 12). When calculating the visibilities for each annulus, we retain the approximation of a geometrically flat inner disk¹ and use Equation 11. Thus, the normalized squared visibilities for this model are computed using Equations 23, 11, 12, and 2.

As discussed in §3.2.2, the fitted inner disk sizes are not particularly sensitive to the choice of T_{in} . However, for the puffed-up inner disk model, fitted sizes will be slightly *smaller* for lower values of T_{in} . The puffed-up inner rim is much hotter than the flared disk component and, as the rim temperature decreases, the difference in flux between the rim and inner disk annuli decreases. This leads to a larger flux-weighted effective area, which, in turn, leads

¹This approximation is valid for the inner disk (where the K-band emission arises) because flaring is negligible in the inner regions. Moreover, the vertical puffing of the inner rim will cause little deviation between the true and approximate visibilities. Even in the edge-on case, the approximation will not be far-off since the minor axis is essentially unresolved in either the true or approximate model.

to smaller fitted sizes (Equation 8). While we have ignored the effect of the shadow cast by the inner rim onto the disk (DDN), this will not significantly alter the results since the fitted sizes are relatively insensitive to the temperature difference between the rim and the disk. We also note that of the two values of T_{in} considered, models with $T_{\text{in}} = 2000$ K have a larger temperature difference between the puffed-up rim and the inner disk annuli, and thus more closely approximate the effects of shadowing.

3.2.4. Binary Model

This model simulates a wide binary, where visibilities are effectively due to two stationary point sources. The squared visibilities for the binary model are,

$$V_{\text{binary}}^2 = \frac{1 + R^2 + 2R \cos\left(\frac{2\pi}{\lambda} \vec{B} \cdot \vec{s}\right)}{(1 + R)^2}, \quad (24)$$

where $(\vec{B} \cdot \vec{s})/\lambda = \theta[u \sin(\psi) + v \cos(\psi)]$, θ is the angular separation of the binary, ψ is the position angle, R is the ratio of the fluxes of the two components, and λ is the observed wavelength.

4. Results and Analysis

4.1. PTI Results

Disk models fit the PTI data reasonably well for most sources in our sample. All sources except HD 141569 and HD 158352 are resolved, with uniform disk diameters between ~ 2.5 and 5.8 mas, and most sources show evidence for non-symmetric circumstellar distributions. While a nearly circularly symmetric distribution appears appropriate for AB Aur, the data for MWC 480, MWC 758, CQ Tau, VV Ser, V1685 Cyg, AS 442, and MWC 1080 show evidence for significantly non-zero inclinations. A high inclination cannot be ruled out for V1295 Aql, and the data for T Ori, MWC 120, and MWC 297 are insufficient to constrain the inclinations.

Tables 4–8 list the fitted parameters and χ_r^2 values for various disk models. Columns 2 and 3 list the χ_r^2 values and best-fit angular size scales (θ) for face-on models, and columns 4–7 list the χ_r^2 , sizes (θ), position angles (ψ), and inclinations (ϕ) for inclined models. The $u - v$ coverage for T Ori, MWC 120, and MWC 297 is insufficient to fit inclined disk models, and for these sources we constrain only the angular size scales of face-on disk models. Table

8, which lists the fitted parameters for flared disk models with puffed-up inner walls, does not include MWC 297, V1685 Cyg, and MWC 1080, the sources with the earliest spectral types in our sample. For these objects, the puffed-up inner wall model cannot fit the visibility data ($\chi_r^2 \gg 100$), since the early-type central stars lead to hot inner disks at radii much larger than allowed by the PTI data.

In Table 9, we present the angular separations (θ), position angles (ψ), and brightness ratios (R) for binary models. The $u - v$ coverage for T Ori, MWC 120, and MWC 297 is insufficient to fit binary models, and these sources are therefore absent from Table 9. The best-fit binary separations for all sources in our sample are $\gtrsim 2.5$ mas. For the distances and approximate masses of the sources in our sample, these separations correspond to orbital periods of $\gtrsim 2$ years. For most objects, observations span several months, and our assumption that the two point sources in the binary model are stationary is reasonable. This assumption may break down for short-period binaries in sources with observations spanning more than 1 year (see Table 2). However, short-period orbits would produce visibilities that vary with time, and no time-variation is detected.

Figures 2–12 show plots of observed V^2 for each source along with the curves predicted by various models. Inclined disk and binary models are not circularly symmetric, and the visibilities are a function of the observed position angle in addition to the projected baseline (Figure 1). Thus, for sources with sufficient data to constrain the inclination, we have plotted V^2 as a function of both r_{uv} and hour angle. Since we were only able to derive lower limits on the angular size scales for MWC 297, we do not plot the models for this source here.

AB Aur, VV Ser, V1685 Cyg, AS 442, and MWC 1080 were discussed in ELAHS. Here, we have obtained additional data on additional baselines for all except MWC 1080, and the greatly enhanced $u - v$ coverage, shown in Figure 1, enables firmer constraints on the models. We include MWC 1080 in the present discussion largely for completeness, since we perform some additional analysis steps that were absent in the first paper.

4.1.1. AB Aur

The PTI visibilities for AB Aur are consistent with a disk-like circumstellar distribution that is nearly face-on (Figure 2). From Tables 4-8, the best-fit models indicate size scales² between 2.2 and 5.3 mas, and an inclination angle between 8° and 16° , consistent with the

²As outlined in §3.2.1–3.2.3, characteristic size scales for different models measure different parts of the brightness distributions: Gaussian models measure full widths at half maxima, uniform disk models measure outer diameters, ring models measure inner ring diameters, and accretion disk models (flat or flared) measure

values found by ELAHS. We have, however, reduced the uncertainties using additional data on a second baseline. The data cannot be fit well by a binary model ($\chi_r^2 \sim 117$; Table 9).

4.1.2. MWC 480

The PTI visibilities for MWC 480 are consistent with a disk inclined by $\sim 30^\circ$, at a position angle of $\sim 150^\circ$ (Figure 3). Specifically, best-fit angular size scales range from 2.0 to 5.0 mas, inclinations range from 24° to 32° , and position angles are between 127° and 155° (Tables 4–8). Inclined fits give $\chi_r^2 \sim 1.4$, significantly lower than the $\chi_r^2 \sim 5.0$ values for face-on models. A binary model can be ruled out with a high degree of confidence ($\chi_r^2 = 13.5$).

4.1.3. MWC 758

The angular size scales for best-fit disk models range from 1.5 to 4.2 mas. Disk inclinations are between 33° and 37° , and position angles vary from 127° to 130° (Tables 4–8). For this source, all parameters are firmly constrained because we obtained data on three baselines. An inclined disk model clearly fits the data better than a face-on model (Figure 4; $\chi_r^2 < 1$ for inclined models, compared to $\chi_r^2 > 3$ for face-on models). A binary model provides a poor fit to the data, with $\chi_r^2 = 5.9$.

4.1.4. CQ Tau

The best-fit angular size scales for CQ Tau are between 1.5 and 4.4 mas. The best-fit inclination is 48° , and position angles range from 104° to 106° (Tables 4–8). All parameters are firmly constrained because we obtained data on three baselines. Inclined model fits give $\chi_r^2 < 1$, while face-on fits have much higher χ_r^2 values, $\gtrsim 5$. A binary model seems unlikely, with $\chi_r^2 = 4.4$.

inner disk diameters. The spread in quoted angular sizes for a source is mainly due to these differences.

4.1.5. *T Ori and MWC 120*

Since we obtained data on only one baseline for T Ori and MWC 120, we are unable to constrain inclinations or position angles. The best-fit angular size scales for T Ori range from 1.1 to 2.7 mas, and the values for MWC 120 are between 2.1 and 4.9 mas (Tables 4–8). The limited uv coverage for these sources does not allow us to rule out (or constrain the parameters of) binary models.

4.1.6. *MWC 297*

This source is extremely resolved, and we are only able to place lower limits on the angular size scales (corresponding to upper limits on the visibilities). We can neither constrain the exact geometry of the emission, nor rule out a binary model. For the face-on disk models discussed above, we find lower-limits on angular size scales of 2.1 to 5.0 mas. As we discuss below, this source has also been resolved by the IOTA interferometer (MST; §4.2), allowing more accurate constraints on angular size. The puffed-up inner disk model does not fit the visibility data for this source, since the flared disk is quite hot even at large radii due to the hotter central star, which leads to an inner disk radius much larger than allowed by the visibility data.

4.1.7. *VV Ser*

The angular size scales for best-fit disk models range from 1.5 to 4.5 mas, disk inclinations are between 42° and 47° , and position angles range from 165° to 173° (Tables 4–8). An inclined disk model clearly fits the VV Ser data better than a face-on model (Figure 8). Inclined model fits give $\chi_r^2 < 1$, while face-on model fits have $\chi_r^2 > 5$ (Table 4–8). However, as indicated in Figure 1, the $u - v$ coverage for this object is somewhat sparse, and a binary model cannot be ruled out ($\chi_r^2 \sim 0.75$; Figure 8).

While the fitted parameters are consistent (within the uncertainties) with those listed in ELAHS, the inclination determined here is significantly lower as a result of new data on an additional baseline. However, we note that we only have one data point on the SW baseline, which makes it difficult to estimate a true error bar, and thus the uncertainties on the fitted parameters may be larger than the statistical uncertainties quoted in Tables 4–8. We emphasize that if the SW data point is excluded from the fit, the inclination is closer to edge-on ($80^\circ - 89^\circ$; ELAHS).

4.1.8. V1295 Aql

The visibilities for V1295 Aql appear consistent with a disk that is close to face-on, although we do not rule out a significantly non-zero inclination. The angular size scales of best-fit models are between 2.4 and 5.6 mas, and inclinations range from 12° to 50° . While there is no discernible difference in the χ_r^2 values for face-on and edge-on disks, the $u - v$ coverage for this source is sparse (Figure 1), and we cannot obtain an accurate estimate of the inclination. We also cannot rule out a binary model (Figure 9).

4.1.9. V1685 Cyg

The size scales for V1685 Cyg under the assumptions of various disk models range from 1.3 to 3.6 mas, the best-fit inclination is 41° , and the best-fit position angle is 110° (Tables 4–8). These parameters are consistent with those found in ELAHS, and we have improved the uncertainties using additional data from a third baseline. The visibility data are not fit very well by any model, although of those considered, inclined disks fit best ($\chi_r^2 \sim 3.9$; Figure 10). $\chi_r^2 = 15$ for a binary model, making this an unlikely choice. The flared disk model with a puffed-up inner wall also does not fit the visibility data for this source, since the flared disk is quite hot even at large radii due to the hotter central star, which leads to an inner disk radius much larger than allowed by the visibility data.

Since none of the models provide very good fits to the data, we attempted to fit several more complex models, including an inclined disk+point source, binary face-on uniform disks, and a model consisting of three point sources. These models reduce the χ_r^2 (to approximately 2.5), but still do not appear to accurately fit all of the visibility data. We speculate that a more complex circumstellar distribution, such as a highly non-uniform disk with multiple hot-spots, may be necessary to explain the observations. Complete understanding of this source may have to wait until multi-baseline interferometers like *IOTA-3T*, *CHARA*, *VLTI*, or *Keck Interferometer* allow synthesis imaging.

4.1.10. AS 442

The PTI data for AS 442 generally have low signal-to-noise, and it is difficult to distinguish between different models. We have added a third baseline to the dataset used in ELAHS, which allows us to make estimates of size scales and inclinations (albeit with large uncertainties). The size scales for various disk models range from 1.0 to 2.7 mas, the inclination ranges from 46° to 48° , and the position angles are between 57° and 59° (Tables 4–8).

While we cannot rule out a face-on disk model, the χ_r^2 values are somewhat lower for the inclined disk models: ~ 0.9 versus ~ 1.0 for face-on models. We cannot rule out a binary model with these data, and in fact, the binary model has the lowest χ_r^2 value of all models considered.

4.1.11. MWC 1080

The PTI visibilities for MWC 1080 are consistent with a disk inclined by $\sim 30^\circ$ (Figure 12). The best-fit angular size scales are between 1.7 and 4.1 mas, inclination angles range from 28° to 40° , and position angles are between 54° and 56° . The χ_r^2 values for inclined models are significantly lower than for face-on disk or binary models. While the uncertainties on position angle and inclination quoted in Tables 4–8 are somewhat large, we show below that when IOTA data is included, the uncertainties are reduced considerably (§4.2). The flared disk model with a puffed-up inner wall does not fit the visibility data for this source since the flared disk is quite hot even at large radii due to the hotter central star, which leads to an inner disk radius much larger than allowed by the visibility data.

4.2. Comparison with K and H-band IOTA Visibilities

Interferometric observations of AB Aur and MWC 1080 at $2.2 \mu\text{m}$ have also been obtained with the 21-m and 38-m baselines of the IOTA interferometer (Millan-Gabet et al. 1999; MST). In ELAHS, we combined this $2.2 \mu\text{m}$ IOTA data with PTI data. However, we misinterpreted the IOTA data in that analysis (confusing V for V^2) such that the plotted IOTA visibilities appeared closer to unity than they actually are. We have rectified that error here. MST also obtained $1.6 \mu\text{m}$ H-band visibilities for AB Aur, T Ori, MWC 297, V1295 Aql, V1685 Cyg, and MWC 1080. Based on discussion with R. Millan-Gabet, we assign an uncertainty to each IOTA visibility given by the standard deviation of all data obtained for a given source with a given baseline.

We compare the visibilities measured by PTI and IOTA for each source by fitting a flat accretion disk model (§3.2.2) to the combined H+K-band dataset³. The best-fit face-on flat accretion disk models are plotted in Figure 13, and the fitted parameters for face-on and

³Since we are interested primarily in the comparison between PTI and IOTA data, the choice of model is not important; we choose the flat accretion disk model because it is computationally simple compared to the puffed-up inner disk model.

inclined disk models are listed in Table 10. Examination of Figure 13 and comparison of Tables 7 and 10 show that the PTI and IOTA data are consistent, and that the combined dataset gives results compatible with those derived from the PTI data alone.

For some sources, there may be a slight trend in the IOTA data toward lower visibilities than the PTI data: this difference is most pronounced for AB Aur, where both the PTI and IOTA data sets are consistent with a nearly face-on disk model, but the IOTA data imply a size that is $\sim 20\%$ larger. We speculate that this discrepancy may be due to the $3''$ field of view of the IOTA interferometer, which is significantly larger than the $1''$ field of view of PTI. Scattered or thermal emission from dust on large scales ($\gtrsim 1''$) might contribute incoherent emission to the IOTA visibilities that is not present in the PTI data, leading to a larger measured size (see §3.1.3). Including a spatially uniform incoherent component via Equation 3, an incoherent flux of $0.6F_* = 1$ Jy leads to a measured size in the IOTA data equal to that measured by PTI. Near-IR and optical imaging have revealed scattered light structures up to $4'' - 9''$ away from AB Aur (Fukagawa et al. 2004; Grady et al. 1999), providing some evidence for (possibly K-band emitting) dust at large radii.

The sizes determined when uniform, incoherent emission is included in the model are $\lesssim 20\%$ larger than the values determined from the IOTA data when incoherent emission is ignored. For the PTI data, this discrepancy is $< 1\%$. Thus, while there may be some uncertainty in the disk sizes determined from the IOTA data, the smaller field of view of PTI should lead to uncertainties of less than a few percent. However, the exact brightness profile of the extended emission is unknown, and thus we cannot quantify precisely the magnitude of the uncertainty for the PTI data. Future measurements with interferometers possessing even smaller fields of view (e.g., *Keck Interferometer* with a 50 mas field of view), when combined with the data discussed here, will constrain further the effects of extended emission on the measured visibilities.

For MWC 1080, while the K-band visibilities from IOTA and PTI are compatible (the fit to the combined dataset gives very similar parameters to those determined in §4), the H-band data appears to be inconsistent with a disk model. This discrepancy was noted by MST, who speculated that the cause might be a resolved calibrator used in the IOTA observations, or possibly increased scattering at shorter wavelengths. Since the K-band data are consistent with a disk model while the H-band data are not, we favor the latter interpretation.

The H-band IOTA visibilities for MWC 297 lead to a size of 3.38 mas. Since our PTI data presented in §4 yielded only an upper limit for the size of this source, we will adopt the size measured by IOTA in the further analysis presented below.

4.3. Binaries

There is always the possibility that the visibilities for some of the observed HAEBE sources may be (partially) due to close companions. For AB Aur, MWC 480, MWC 758, CQ Tau, V1685 Cyg, and MWC 1080, we can rule out binary models (with separations $\gtrsim 1$ mas) with a high degree of confidence based on the near-IR visibility data (Table 9). The stability of the visibilities over a long time baseline (> 1 year) for AB Aur and V1685 Cyg supports this conclusion. However, MWC 1080 is known to be an eclipsing binary with a period of $P \approx 2.9$ days (Shevchenko et al. 1994; Herbst & Shevchenko 1999), and T Ori is an eclipsing spectroscopic binary with a period of approximately 14 days (Shevchenko & Vitrichenko 1994). These orbital separations are much too small to be detected by PTI, and the observed visibilities for these sources are thus probably due to circum-*binary* disks. As yet, the binarity status of MWC 120, MWC 297, V1295 Aql, AS 442, and VV Ser remains uncertain based on our visibility data. Radial velocity variations of spectral lines in AS 442 have been attributed to a binary with $P \approx 64$ days and $e \approx 0.2$, while a lack of spectral line variation in V1295 Aql suggests a single source (Corporon & Lagrange 1999).

4.4. Spectral Energy Distributions

The inner disk sizes and inclinations determined from our near-IR interferometry data directly constrain common models of the spectral energy distributions (SEDs) for HAEBEs. The derived inner radii constrain the structure of the inner disks, while the inclination estimates provide constraints on the structure of the entire disks (assuming the disks are not significantly warped; see §5.3). For the geometrically flat accretion disk model discussed in §3.2.2 and the flared disk model with a puffed-up inner wall discussed in §3.2.3, we compute the SEDs for our best-fit inner disk parameters (Tables 7 and 8; Table 10 for MWC 297). For T Ori, MWC 120, and MWC 297, which do not have inclination estimates, we assume an inclination of zero. The model SEDs are plotted in Figures 14 and 15.

We compare these predicted SEDs to actual measurements compiled from new data (§2.1) and the literature (Herbst & Shevchenko 1999; Hillenbrand et al. 1992; de Winter et al. 2001; Malfait et al. 1998; Oudmaijer et al. 1992; Vieira et al. 2003). Although photometry from the literature often lacks error bars, typical uncertainties are ~ 0.05 – 0.1 mag for wavelengths $< 10 \mu\text{m}$ and $\sim 10\%$ at longer wavelengths. Source variability may lead to additional errors since photometric observations (at different wavelengths) often span several years. Since we cannot quantify the uncertainties, we do not include them in our analysis of the SEDs.

For the geometrically flat disk model, the most important parameter beside R_{in} and

inclination is T_{in} (Equation 10). As discussed in §3.2.2, the fitted inner radius depends very slightly on T_{in} . However, as illustrated by Figure 14, which shows the SEDs predicted for different values of T_{in} , this parameter has a significant effect on the SED. The other free parameter in the flat disk model is R_{out} , which is relatively unimportant since most of the flux at wavelengths < 1 mm is generated in the inner regions of the disk (< 50 AU). We vary T_{in} between 1000 K and 2500 K (in increments of 10 K) and use a least squares technique to determine the value that provides the best fit to the measured SED (considering only the SED long-ward of $1 \mu\text{m}$, since we are interested in the circumstellar emission). The best-fit R_{in} and T_{in} values for this model are listed in Table 11.

For the flared disk model with a puffed-up inner wall, several parameters may affect the predicted SED: T_{in} , R_{out} , $\Sigma(R)$, $\kappa(\nu)$, and the flaring index, ξ (Equations 18, 20, and 22). For simplicity, we will retain our initial assumptions about Σ and κ , and attempt to find the values of T_{in} , ξ , and R_{out} that give the best fit of the model to the observed SEDs (again, considering the SED only long-ward of $1 \mu\text{m}$). Specifically, we use a least squares fitting method, varying T_{in} from 1000 to 2500 K in 10 K increments, ξ from 0.10 to 0.28 in increments of 0.02, and R_{out} from 30 to 400 AU in 10 AU increments. We note that varying ξ qualitatively corresponds to changing the overall flaring of the disk, and while slight modifications to Equation 13 may be necessary when ξ is changed, we ignore those here. Since we can rule out the flared, puffed-up inner disk model for MWC 297, V1685 Cyg, and MWC 1080 on the basis of the near-IR visibility data alone (§4.1), we do not attempt to fit the SEDs for these sources. The best-fit R_{in} , T_{in} , ξ , and R_{out} values for the remaining sources are listed in Table 11.

From Figure 14, we see that with the parameters derived from the near-IR interferometry (inner radius and inclination), geometrically flat accretion disk models can fit the SEDs reasonably well for some sources. The best fits are achieved for MWC 297, V1685 Cyg, and MWC 1080, the sources with the earliest spectral types in our sample. The far-IR photometry for these objects appears somewhat inconsistent with the models, perhaps due to tenuous dust halos, or possibly due to source confusion in the large IRAS beams (not unlikely given that these higher-mass stars are found in small stellar clusters). For these early-type sources, we also find that the near-IR visibility data is completely inconsistent with the predictions of flared disk models with puffed-up inner walls.

For the other nine sources in our sample, which all have spectral types later than B9, the SEDs are generally fit well by flared disk models with puffed-up inner walls (Figure 15). However, while the puffed-up inner disk wall generally fits the near-IR data well, for CQ Tau and T Ori the model does not fit the long-wavelength data. Although this disagreement may be lessened for T Ori using a non-zero inclination (we assumed a face-on

disk since no inclination estimate is available from our near-IR interferometry), the outer disk structure of CQ Tau is inconsistent with the model. Moreover, many of the sources in our sample require flaring angles smaller than those predicted by standard flared-disk models (i.e., $\xi < 2/7$), which could support the contention of DDN that shadowing by the inner rim plays a prominent role in the outer disk structure of HAEBEs.

Motivated by Monnier & Millan-Gabet (2002), we explore the apparently different disk structure for early and late-type HAEBEs from a different perspective in Figure 16, where we plot the ratio of predicted to measured inner disk size as a function of stellar luminosity for the two different disk models. The predicted inner disk size is computed by assuming the disk is heated only by stellar radiation (i.e., no accretion), and using the structure equations for flat or puffed-up inner disks (see ELAHS) to determine the radius where $T = T_{\text{in}}$. For each source, T_{in} is the value determined from the SED (Table 11). The measured size is calculated from the angular size determined for either a flat inner disk model (§3.2.2) or a puffed-up inner disk wall model (§3.2.3) and the distance assumed in Table 1. Since the predicted and measured sizes are both directly proportional to distance (ELAHS), the ratio is independent of the assumed distance. Thus, Figure 16 is effectively testing whether the inner disk sizes determined from the near-IR interferometric data are consistent with the disk temperatures implied by the stellar parameters. While stellar variability may complicate the interpretation of this diagram, the general trends should be unaffected.

Figure 16 shows that for later-type sources, the predicted inner disk sizes are within a few tens of percent of the measured values for puffed-up inner disk models, while flat disk models are off by a factor of approximately 2. In contrast, the predictions of flat models are reasonably close to measured values for early-type sources, while the puffed-up inner disk models predict inner disk sizes much larger (factors $\gtrsim 5$) than allowed by the data. Including accretion luminosity in flat disk models will lead to warmer inner disk temperatures and thus larger predicted inner radii, in better agreement with the measurements. While this argues for flat disk models with accretion in early-type Herbig Be stars, the SEDs demonstrate that puffed-up inner disk models still provide superior fits for the later-type sources.

5. Discussion

Our new PTI results strengthen the arguments supporting the existence of circumstellar disks around HAEBE stars presented in §1. Resolved, small-scale (~ 1 AU) distributions of dust are found in all observed sources except HD 141569 and HD 158352, and the non-symmetric intensity distributions of best-fit models for most objects provide support for inclined disk geometries.

5.1. Unresolved Sources

HD 141569 and HD 158352 show no evidence of near-IR emission in excess of that expected for the stellar photospheres, and thus it is not surprising that we did not resolve any circumstellar emission with PTI. Rather, our PTI observations imply uniform disk radii $\lesssim 10 R_{\odot}$, consistent with the near-IR emission arising in the stellar photospheres for these sources. Although HD 141569 is surrounded by a circumstellar disk, it appears to have a central gap extending out to $\sim 17 - 30$ AU (Brittain et al. 2003; Marsh et al. 2002; Weinberger et al. 1999; Augereau et al. 1999; Sylvester & Skinner 1996), which explains the lack of near-IR excess emission. Moreover, millimeter observations imply a very low dust mass, suggesting that this system is more evolved than other members of the HAEBE class (Sylvester et al. 2001). Although HD 158352 was listed as a candidate HAEBE by Thé, de Winter, & Pérez. (1994), recent observations suggest that it may in fact be a more evolved source, such as a shell star or Vega-like object (Grady et al. 1996; Eritsyan et al. 2002). Thus, it appears that HD 141569 and HD 158352 are probably more evolved than most HAEBE sources (including the remainder of our sample), which may explain the lack of near-IR circumstellar emission for these objects.

5.2. Disk Inclinations

The inclination estimates determined from near-IR interferometric data are generally compatible with inclinations inferred from other observations. Our interferometric measurements show that the resolved circumstellar material around MWC 480, MWC 758, CQ Tau, VV Ser, V1685 Cyg, AS 442, and MWC 1080 is significantly inclined. Large-amplitude flux and color variability in CQ Tau ($\Delta V \sim 2$ mag), VV Ser ($\Delta V \sim 2$ mag), V1685 Cyg ($\Delta V \sim 1$ mag), and AS 442 ($\Delta V \sim 1$ mag), which has been attributed to variable obscuration from clumps of dust orbiting in inclined circumstellar disks (Herbst & Shevchenko 1999), provides support for this high inclination distribution. Furthermore, high inclinations are suggested by resolved mm emission for MWC 480, MWC 758, and CQ Tau (§5.3), by optical polarization measurements for CQ Tau (Natta & Whitney 2000), and by ro-vibrational CO emission for MWC 480, MWC 758, and VV Ser (Blake & Boogert 2004). However, the broad, double-peaked line profile of ro-vibrational CO emission from VV Ser suggests an inner disk inclination higher than the $\sim 45^{\circ}$ estimate presented here. As described in §4.1.7, the lower inclination estimate depends on a single data point, and if this point is excluded, we obtain an inclination of $\sim 85^{\circ}$, consistent with the CO observations.

The PTI data for AB Aur are consistent with a circumstellar distribution that is within 20° of face-on. Other data for AB Aur support this contention, including near-IR inter-

ferometric results (MST, §4.2), ro-vibrational CO emission (Blake & Boogert 2004), resolved millimeter emission (§5.3), scattered optical and near-IR light (Grady et al. 1999; Fukagawa et al. 2004), and small amplitude optical variability ($\Delta V \sim 0.25$; Herbst & Shevchenko 1999). We also note that the inner disk size for AB Aur determined above is consistent with recent observations of ro-vibrational emission from hot CO gas, which show that the CO lies near to, but somewhat behind the inner disk boundary. Moreover, the CO emission is found only in the lowest vibrational state, suggesting that the hot gas is shielded from stellar UV radiation, perhaps by a puffed-up inner disk wall (Brittain et al. 2003; Blake & Boogert 2004).

While the V1295 Aql data seems consistent with a nearly face-on circumstellar distribution, we cannot rule out a high inclination value for this source based on the PTI data alone. The data for T Ori, MWC 120, and MWC 297 are insufficient to constrain the inclinations.

5.3. Inner versus Outer Disk Structure

Our PTI results probe dust in the inner (< 1 AU) disk, while millimeter interferometric observations probe dust and gas in the outer ($\gtrsim 100$ AU) disks of HAEBE stars. Comparison of these observations enables constraints on disk warping. Of our sample, inclinations are available from millimeter CO observations for AB Aur, CQ Tau, MWC 480, and MWC 758 (Mannings & Sargent 1997; Mannings et al. 1997; Mannings & Sargent 2000; Simon et al. 2001; Testi et al. 2003; Corder et al. 2004).

As discussed in earlier papers (MST; ELAHS), the inclination for AB Aur estimated from the aspect ratio of resolved millimeter CO emission, $i = 76^\circ$ (Mannings & Sargent 1997), is inconsistent with the lower inclinations from near-IR interferometry ($i \lesssim 20^\circ$; ELAHS) and modeling of scattered light emission ($i < 30^\circ - 45^\circ$; Fukagawa et al. 2004; Grady et al. 1999). This suggests that the disk around AB Aur may be significantly warped, which is difficult to explain theoretically. However, more detailed kinematic modeling of millimeter observations with higher angular resolution and sensitivity find an outer disk around AB Aur inclined by $\lesssim 30^\circ$ (Corder et al. 2004; Natta et al. 2001), compatible with our near-IR results.

For CQ Tau, the aspect ratio estimated from VLA data at 7mm implies an inclination angle ($\sim 70^\circ$; Testi et al. 2003) somewhat larger than that determined from near-IR interferometry ($\sim 48^\circ$; §4.1.4). Kinematic modeling of more sensitive millimeter observations shows that the outer disk is actually inclined by $\sim 45^\circ$ (Corder et al. 2004), consistent with our PTI results.

For MWC 480, there is some variation in the outer disk geometry based on different observations. A Keplerian model fit to one set of millimeter CO observations yields an

inclination and position angle of $\sim 30^\circ$ and $157^\circ \pm 4^\circ$, respectively (Mannings et al. 1997), while another gives $38^\circ \pm 1^\circ$ and $148^\circ \pm 1^\circ$ (Simon et al. 2001). The millimeter continuum, which traces cool dust, gives yet another estimate of geometry; $i = 26^\circ \pm 7^\circ$, $pa = 170^\circ \pm 11^\circ$ (Simon et al. 2001). We compare these with estimates of the inner disk geometry from our PTI results: $i = 24^\circ - 32^\circ$, $pa = 149^\circ - 156^\circ$. Since the outer disk geometry estimates vary considerably, it is difficult to estimate the true uncertainty in inclination. However, it seems reasonable to say that the various observations are consistent with no offset at all, and that there is at most a difference of 15° between the inner and outer disk. While there is an intriguing hint that the dust may be somewhat less inclined than the gas, we cannot verify this possibility with the current data.

Finally, for MWC 758, the aspect ratio of millimeter CO emission implies a disk inclined by 46° at a position angle of 116° (Mannings & Sargent 1997). For comparison, the PTI measurements imply an inclination of $33^\circ - 37^\circ$ and a position angle of $127^\circ - 130^\circ$. There is some spread between these estimates, but again, it seems that there is a difference of $\lesssim 10^\circ$ between the inner and outer disk inclinations.

For the 4 sources in our sample that have inner and outer disk geometry measurements, there is little evidence for inner and outer disk mis-alignments of more than a few degrees. Thus, the inner disk geometries derived from our PTI data likely describe the structure of the entire disks. While we do not rule out small warps (up to ~ 10 degrees), such as those expected from resonant interactions with giant planets or magnetic warping (e.g., Mouillet et al. 1997; Lai 1999), our results argue against significant perturbation due to massive companions (e.g., Bate et al. 2000), consistent with the lack of binaries in our visibility and adaptive optics data.

5.4. Vertical Disk Structure

Figures 14 and 15 demonstrate that flared, puffed-up inner disk models tend to fit the SEDs better than geometrically flat accretion disk models for later-type HAEBE sources, while flat disk models fit the visibility and SED data well for early-type Herbig Be sources. Moreover, Figure 16 clearly demonstrates that puffed-up inner disk models more accurately predict the inner radii of late-type HAEBEs, while geometrically flat disk models are far more accurate for early-type sources.

We have already suggested (ELAHS, see also Vink et al. 2002) that the apparent difference between inner disk geometries for early and late-type HAEBEs may be due to a transition from disk accretion (Lynden-Bell & Pringle 1974) in early-type stars to magneto-spheric

accretion (Koenigl 1991) in later-type stars. There is abundant evidence for magneto-spheric accretion in T Tauri stars (Hartmann 1998, and references therein), and it is plausible that the same accretion mechanism would apply to the more massive Herbig Ae stars. Magneto-spheric accretion provides a mechanism for truncating the disks around HAEBE stars, which is necessary to obtain puffed-up inner disk walls (disk truncation allows direct irradiation of the inner disk regions, leading to higher temperatures and thus larger scale heights). In contrast, for earlier spectral types, such as the Herbig Be stars, higher accretion rates and/or weaker stellar magnetic fields may allow the accretion flow to overwhelm the magnetic field, leading to disk accretion down to the stellar surface.

6. Summary

Our new $2.2\ \mu\text{m}$ observations of 14 HAEBE sources have the best $u - v$ coverage of any near-IR interferometric observations of young stellar objects to date. As a result, we accurately constrain the sizes and basic geometries of the material around HAEBEs, providing strong evidence for inner circumstellar disks.

We determine the angular size scales and orientations predicted by uniform disk models, Gaussian models, uniform ring models, geometrically flat accretion disk models with inner holes, and flared passive disk models with puffed-up inner rims. All except two sources are resolved, with angular sizes ranging from $\sim 1.0 - 5.8$ mas. AB Aur appears to be surrounded by a disk inclined by $\lesssim 20^\circ$, while MWC 480, MWC 758, CQ Tau, VV Ser, V1685 Cyg, AS 442, and MWC 1080 are associated with more highly inclined circumstellar disks ($\sim 30 - 50^\circ$). We cannot rule out a high inclination for V1295 Aql, although the data can be explained by a face-on disk model. For T Ori, MWC 120, and MWC 297, the $u - v$ coverage is too sparse to enable constraints on the inclination of the circumstellar material. There is little supporting evidence that our data result from binaries, although we cannot rule out binary models for T Ori, MWC 120, MWC 297, V1295 Aql, AS 442, or VV Ser.

Comparison of our $2.2\ \mu\text{m}$ PTI visibilities with $1.6\ \mu\text{m}$ and $2.2\ \mu\text{m}$ visibilities from the IOTA interferometer (MST) shows that the two datasets are consistent, and allows firmer constraints on circumstellar geometry. Since IOTA has a field of view three times larger than PTI, we are also able to constrain the degree to which incoherent emission from extended dust may bias the measured sizes toward larger values. The smaller field of view of PTI leads to very small biases, and the resulting uncertainties in the measured sizes are likely less than a few percent.

We constrain warping of HAEBE disks by comparing our near-IR measurements of

the inner disks with resolved millimeter interferometric measurements of the outer disk geometries (where available). Our results for 4 sources indicate that the inner and outer disks of HAEBEs are not significantly mis-aligned. While this argues against significant perturbations to the disks, we do not rule out small warps such as those due to interactions between disks and slightly non-coplanar giant planets.

Our measurements also enable constraints on the vertical structure of HAEBE disks. Using the derived inner disk parameters, we compute the SEDs for flat accretion disk models with inner holes and flared passive disk models with puffed-up inner walls, and compare these with measured SEDs for our sample. Geometrically flat disk models fit the data well for the early-type Herbig Be stars in our sample, MWC 297, V1685 Cyg and MWC 1080, while the flared, puffed-up inner disk models cannot fit the data for these objects. In contrast, flared disk models with puffed-up inner rims provide superior fits to the data for the later-type stars in our sample. The different inner disk geometries may imply a transition from magneto-spheric accretion in late-type HAEBEs to disk accretion in early-type sources.

Acknowledgments. The new near-IR interferometry data presented in this paper were obtained at the Palomar Observatory using the Palomar Testbed Interferometer, which is supported by NASA contracts to the Jet Propulsion Laboratory. Science operations with PTI are possible through the efforts of the PTI Collaboration (<http://pti.jpl.nasa.gov/ptimembers.html>) and Kevin Rykoski. This research made use of software produced by the Michelson Science Center at the California Institute of Technology. This publication makes use of data products from the Two Micron All Sky Survey, which is a joint project of the University of Massachusetts and the Infrared Processing and Analysis Center, funded by the National Aeronautics and Space Administration and the National Science Foundation. 2MASS science data and information services were provided by the Infrared Science Archive (IRSA) at IPAC. We thank R. Millan-Gabet for providing us with the IOTA data, for useful discussion, and for a critical review of the manuscript. We are also grateful to S. Metchev for his assistance with the adaptive optics observing and data reduction. J.A.E. is supported by a Michelson Graduate Research Fellowship, and B.F.L. acknowledges support from a Pappalardo Fellowship in Physics.

REFERENCES

Akeson, R.L., Ciardi, D.R., van Belle, G.T., Creech-Eakman, M.J., & Lada, E.A. 2000, *Ap. J.*, 543, 313

- Augereau, J.C., Lagrange, A.M., Mouillet, D., & Ménard, F. 1999, *A&A*, 350, L51
- Bate, M. R., Bonnell, I. A., Clarke, C. J., Lubow, S. H., Ogilvie, G. I., Pringle, J. E., & Tout, C. A. 2000, *M.N.R.A.S.*, 317, 773
- Bigay, J.H., & Garnier, R. 1970, *A&AS*, 1, 15B
- Blake, G.A., & Boogert, A.C.A. 2004, *Ap. J.*, 606, L73
- Brittain, S. D., Rettig, T. W., Simon, T., Kulesa, C., DiSanti, M. A., & Dello Russo, N. 2003, *Ap. J.*, 588, 535
- Chiang, E.I., & Goldreich, P. 1997, *Ap. J.*, 490, 368
- Clampin, M., et al. 2003, *AJ*, 126, 385
- Colavita, M.M., et al. 1999, *Ap. J.*, 510, 505
- Colavita, M.M. 1999, *PASP*, 111, 111
- Corcoran, M., & Ray, T.P. 1997, *A&A*, 321, 189
- Corder, S.A., Eisner, J.A., & Sargent, A.I. 2004, in prep.
- Corporon, P., & Lagrange, A.-M. 1999, *A&AS*, 136, 429
- Corporon, P. 1998, Ph.D. thesis, Univ. Joseph Fourier de Grenoble
- Danchi, W.C., Tuthill, P.G., & Monnier, J.D. 2001, *Ap. J.*, 562, 440
- de Winter, D., van den Ancker, M.E., Maira, A., Thé, P.S., Djie, H.R.E, Tjin, A., Redondo, I., Eiroa, C., & Molster, F.J. 2001, *A&A*, 380, 609
- de Lara, E., Chavarría-K., C., & López-Molina, G. 1991, *A&A*, 243, 139
- Draine, B. T. & Lee, H. M. 1984, *Ap. J.*, 285, 89
- Dullemond, C.P., Dominik, C., & Natta, A. 2001, *Ap. J.*, 560, 957 (DDN)
- Eiroa, C., et al. 2002, *A&A*, 384, 1038
- Eiroa, C., et al. 2001, *A&A*, 365, 100
- Eisner, J.A., Lane, B.F. Akeson, R.L., Hillenbrand, L.A., & Sargent, A.I. 2003, *Ap. J.*, 588, 360 (ELAHS)

- Eritsyan, M.A., Hovhannessian, R. Kh., & Hovhannessian, E.R. 2002, *Astrophys.*, 45, 25
- Fukagawa, M., et al. 2004, *Ap. J.*, 605, L53
- Grady, C.A., Woodgate, B., Bruhweiler, F.C., Boggess, A., Plait, P., Lindler, D.L., Clampin, M., & Kalas, P. 1999, *Ap. J.*, 523, L151
- Grady, C.A., Pérez, M.R., Talavera, A., McCollum, B., Rawley, L.A., England, M.N., & Schlegel, M. 1996, *Ap. J.*, 471, L49
- Hartmann, L., Kenyon, S.J., & Calvet, N. 1993, *Ap. J.*, 407, 219
- Hartmann, L. 1998, *Accretion processes in star formation*, Cambridge University Press, Cambridge astrophysics series 32, p.116
- Hayward, T.L., Brandl, B., Pirger, B., Blacken, C., Gull, G.E., Schoenwald, J., & Houck, J.R. 2001, *PASP*, 113, 105
- Herbig, G.H. 1960, *ApJS*, 4, 337
- Herbst, W., & Shevchenko, V.S. 1999, *Ap. J.*, 118, 1043
- Hillenbrand, L.A., Strom, S.E., Vrba, F.J., & Keene, J. 1992, *Ap. J.*, 397, 613
- Koenigl, A. 1991, *Ap. J.*, 370, L39
- Lai, D. 1999, *Ap. J.*, 524, 1030
- Lynden-Bell, D., & Pringle, J.E. 1974, *M.N.R.A.S.*, 168, 603
- Malfait, K., Bogaert, E., & Waelkens, C. 1998, *A&A*, 331, 211
- Mannings, V., & Sargent, A.I. 2000, *Ap. J.*, 529, 391
- Mannings, V., & Sargent, A.I. 1997, *Ap. J.*, 490, 792
- Mannings, V., Koerner, D.W., & Sargent, A.I. 1997, *Nature*, 388, 555
- Marsh, K.A., Silverstone, M.D., Becklin, E.E., Koerner, D.W., Werner, M.W., Weinberger, A.J., & Ressler, M.E. 2002, *Ap. J.*, 573, 425
- Millan-Gabet, R., Schloerb, F.P., & Traub, W.A. 2001, *Ap. J.*, 546, 358 (MST)
- Millan-Gabet, R., Schloerb, F.P., Traub, W.A., Malbet, F., Berger, J.P., & Bregman, J.D. 1999, *Ap. J.*, 513, L131

- Monnier, J.D., & Millan-Gabet, R. 2002, *Ap. J.*, 579, 694
- Mora, A., et al. 2001, *A&A*, 378, 116
- Mouillet, D., Larwood, J. D., Papaloizou, J. C. B., & Lagrange, A. M. 1997, *M.N.R.A.S.*, 292, 896
- Natta, A., Prusti, T., Neri, R., Wooden, D., Grinin, V.P., & Mannings, V. 2001, *A&A*, 371, 186
- Natta, A., Grinin, V.P., & Mannings, V. 2000, *Protostars and Planets IV*, 559
- Natta, A., & Whitney, B.A. 2000, *A&A*, 364, 633
- Oudmaijer, R.D., et al. 2001, *A&A*, 379, 564
- Oudmaijer, R.D., et al. 1992, *A&AS*, 92, 6250
- Piétu, V., Dutrey, A., & Kahane, C. 2003, *A&A*, 398, 565
- Pollack, J. B., Hollenbach, D., Beckwith, S., Simonelli, D. P., Roush, T., & Fong, W. 1994, *Ap. J.*, 421, 615
- Salpeter, E. E. 1977, *ARA&A*, 15, 267
- Shevchenko, V.S., Grankin, N., Ibragimov, M.B., Kondratiev, V.Y., & Melnikov, S. 1994, in “The nature and evolutionary status of Herbig Ae/Be stars, eds. P.S. Thé, M.R. Pérez, & E.P.J. van den Heuvel, 62, 43
- Shevchenko, V.S., & Vitrichenko, E.A. 1994, in “The nature and evolutionary status of Herbig Ae/Be stars” Thé, P.S., Pérez, M.R., and van den Heuvel, E.P.J. (eds.), 62, 55
- Shevchenko, V.S., Ibragimov, M.A., & Chernysheva, T.L. 1991, *SvA*, 35, 229
- Simon, M., Dutrey, A., & Guilloteau, S. 2001, *Ap. J.*, 545, 1034
- Skrutskie, M.F., Meyer, M.R., Whalen, D., & Hamilton, C. 1996, *AJ*, 112, 2168
- Steenman, H., & Thé, P.S. 1991, *Ap&SS*, 184, 9
- Sylvester, R.J., Dunkin, S.K., & Barlow, M.J. 2001, *M.N.R.A.S.*, 327, 133
- Sylvester, R.J., & Skinner, C.J. 1996, *M.N.R.A.S.*, 283, 457

- Thé, P. S., de Winter, D., & Pérez, M. R. 1994, *A&AS*, 104, 315
- Testi, L., Natta, A., Shepherd, D.S., & Wilner, D.J. 2003, *A&A*, 403, 323
- Troy, M., Dekany, R.G., Brack, G., Oppenheimer, B.R., Bloemhof, E.E., Tring, T., Dekens, F.G., Shi, F., Hayward, T.L., & Brandl, B. 2000, *Proc. SPIE*, 4007, 31
- Tuthill, P.G., Monnier, J.D., Danchi, W.C., Hale, D.D.S., & Townes, C.H. 2002, *Ap. J.*, 577, 826
- Vieira, S.L.A., Corradi, W.J.B., Alencar, S.H.P., Mendes, L.T.S., Torres, C.A.O., Quast, G.R., Guimarães, M.M., & da Silva, L. 2003, *AJ*, 126, 2971
- Vink, J.S., Drew, J.E., Harries, T.J., & Oudmaijer, R.D. 2002, *M.N.R.A.S.*, 337, 356
- Vinković, D., Ivezić, Z., Miroshnichenko, A.S., & Elitzur, M. 2003, *M.N.R.A.S.*, 346, 1151
- Warren, W. H. & Hesser, J. E. 1978, *ApJS*, 36, 497
- Weinberger, A.J., Rich, R.M., Becklin, E.E., Zuckerman, B., & Matthews, K. 2000, *Ap. J.*, 544, 937
- Wilkin, F. P. & Akeson, R. L. 2003, *Ap&SS*, 286, 145

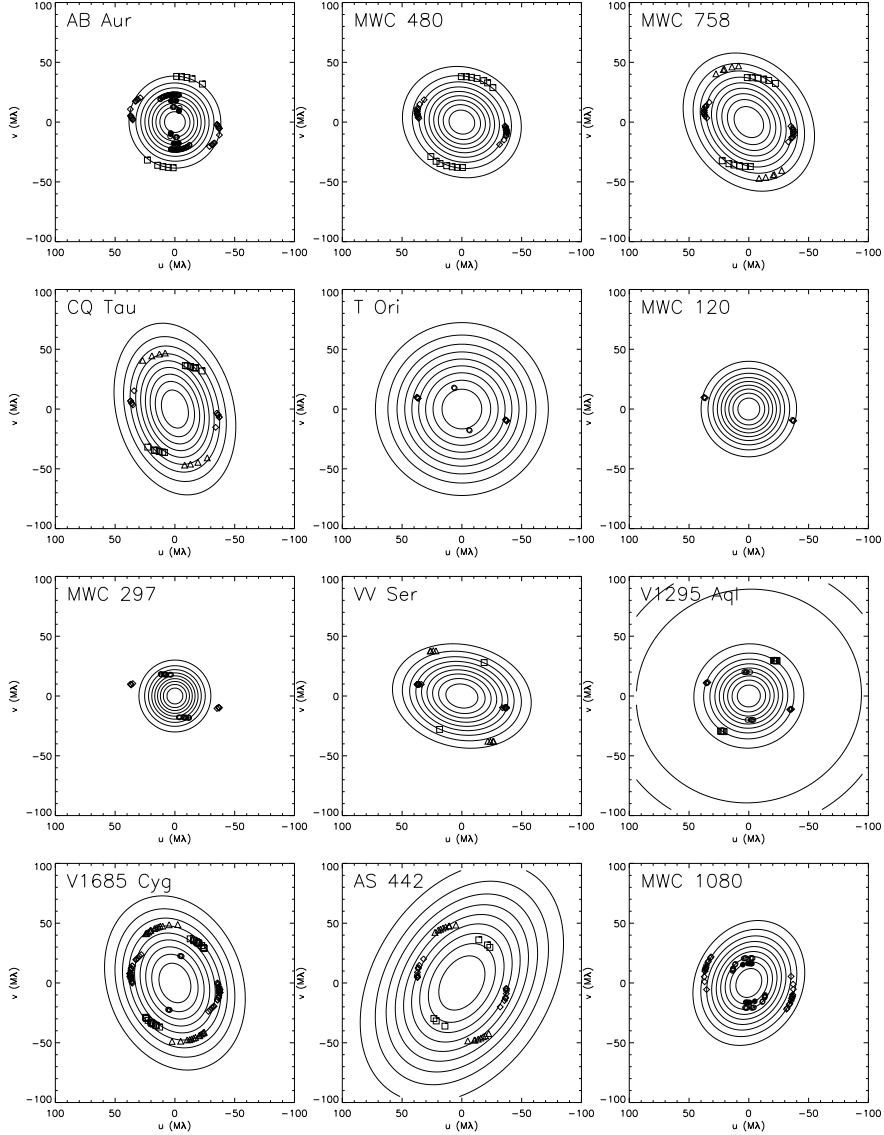


Fig. 1.— Contour plots of best-fit uniform disk models for AB Aur, MWC 480, MWC 758, CQ Tau, T Ori, MWC 120, MWC 297, VV Ser, V1295 Aql, V1685 Cyg, AS 442, and MWC 1080, whose parameters are listed in Table 4. We plot the best-fit inclined models except for T Ori, MWC 120, and MWC 297, where no inclination estimates are available, in which case we use the best-fit face-on models. For MWC 297, we have used the model determined from a combined fit to PTI+IOTA data (§4.2; Table 10), since the PTI visibilities only provide limits. The contour increment is 10% in V^2 . We also plot the $u - v$ points sampled for each source by the PTI NW baseline (open diamonds), the PTI SW baseline (open squares), the PTI NS baseline (open triangles), and by IOTA (MST; H and K-band data, represented by open and filled circles, respectively).

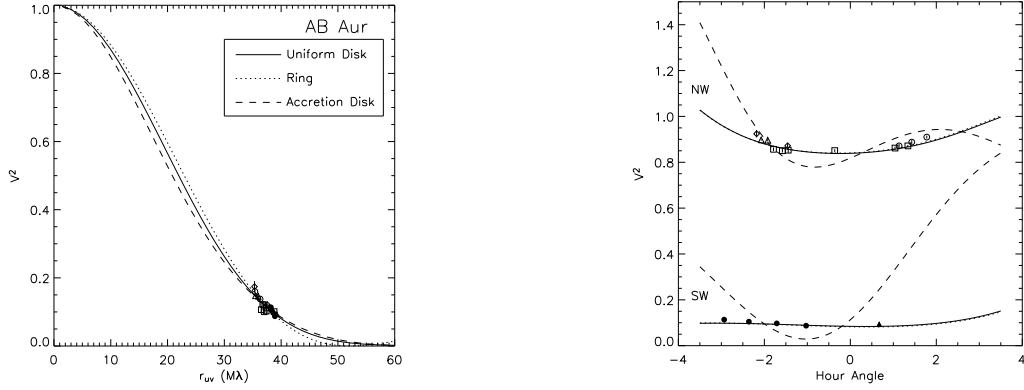


Fig. 2.— V^2 PTI data for AB Aur, as a function of $r_{uv} = (u^2 + v^2)^{1/2}$ (left panel). Data for individual nights are represented by different symbols, where NW data are plotted with open symbols, and SW data use filled symbols. Face-on uniform disk (solid line), ring (dotted line), and geometrically flat accretion disk (dashed line) models are over-plotted. We also plot the data as a function of hour angle (right panel). For clarity, we have plotted $V^2 + 0.75$ for the NW data. The best-fit face-on uniform disk is plotted as a solid line, the best-fit inclined uniform disk model is represented with a dotted line, and the best-fit binary model is shown with a dashed line. We note that the different linestyles correspond to different models in the left and right panels. For this source, we see that a face-on model provides the best fit to the data.

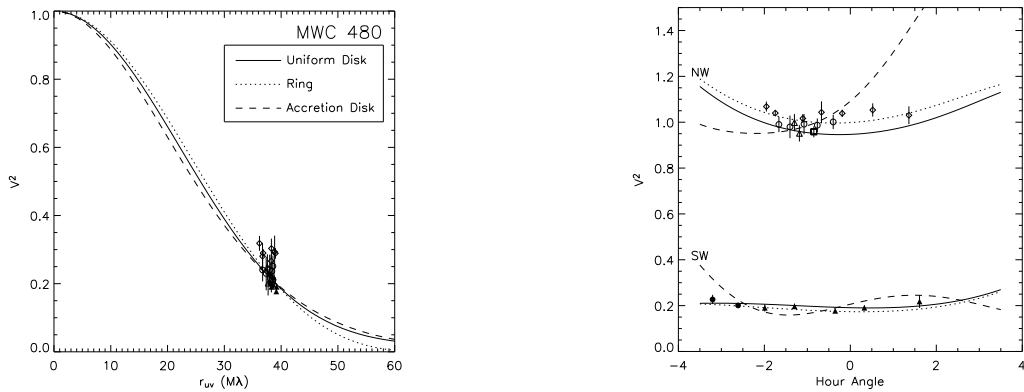


Fig. 3.— V^2 PTI data for MWC 480, as a function of r_{uv} (left panel) and hour angle (right panel). Symbols and models are plotted as in Figure 2. For this source, we see that an inclined disk model provides the best fit to the data.

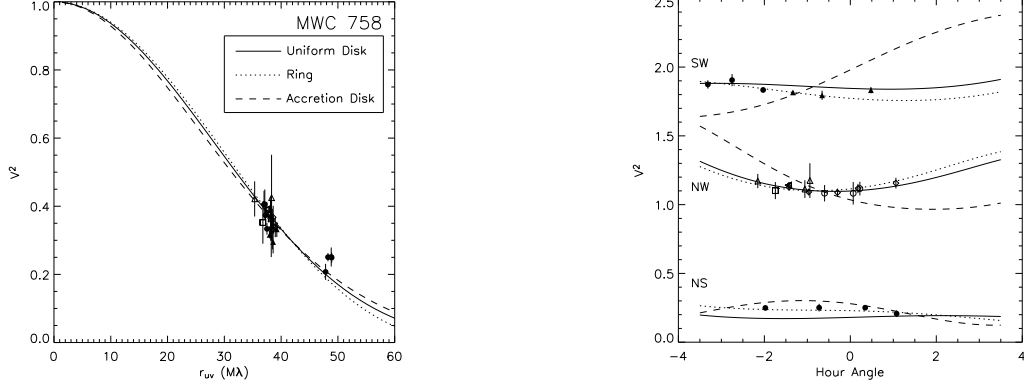


Fig. 4.— V^2 PTI data for MWC 758, as a function of r_{uv} (left panel) and hour angle (right panel). Symbols and models are plotted as in Figure 2, except that here, we have three baselines. NW data are plotted with open symbols, and NS and SW data use filled symbols. In the right panel, we have plotted $V^2 + 0.75$ for the NW data and $V^2 + 1.5$ for the SW data. An inclined disk model provides the best fit to the data.

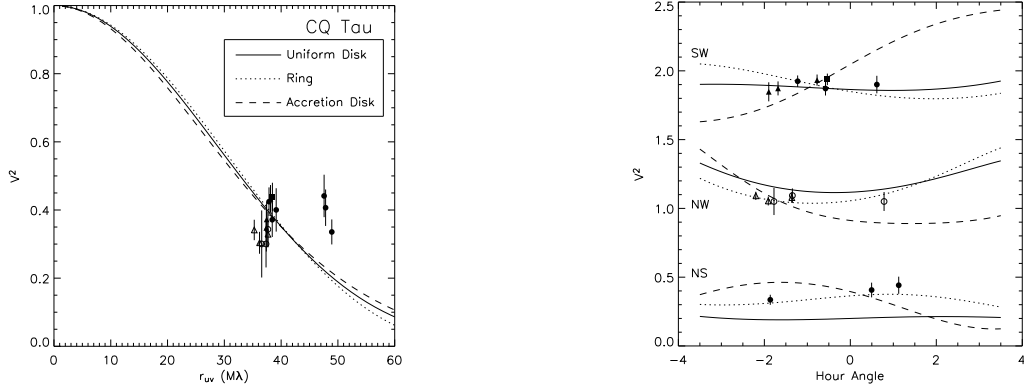


Fig. 5.— V^2 PTI data for CQ Tau, as a function of r_{uv} (left panel) and hour angle (right panel). Symbols and models are plotted as in Figure 4. For this source, an inclined disk model provides the best fit to the data.

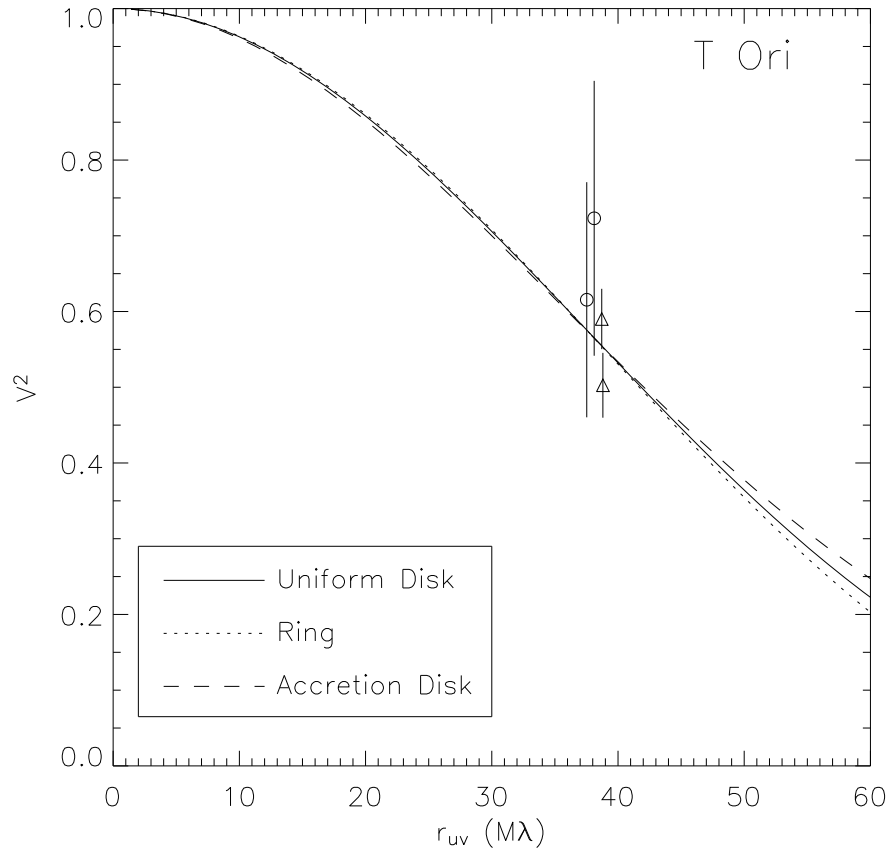


Fig. 6.— V^2 PTI data for T Ori, as a function of r_{uv} . Symbols and models are plotted as in Figure 2. For this source, the limited $u - v$ coverage does not allow an estimate of inclination, so we plot only face-on models.

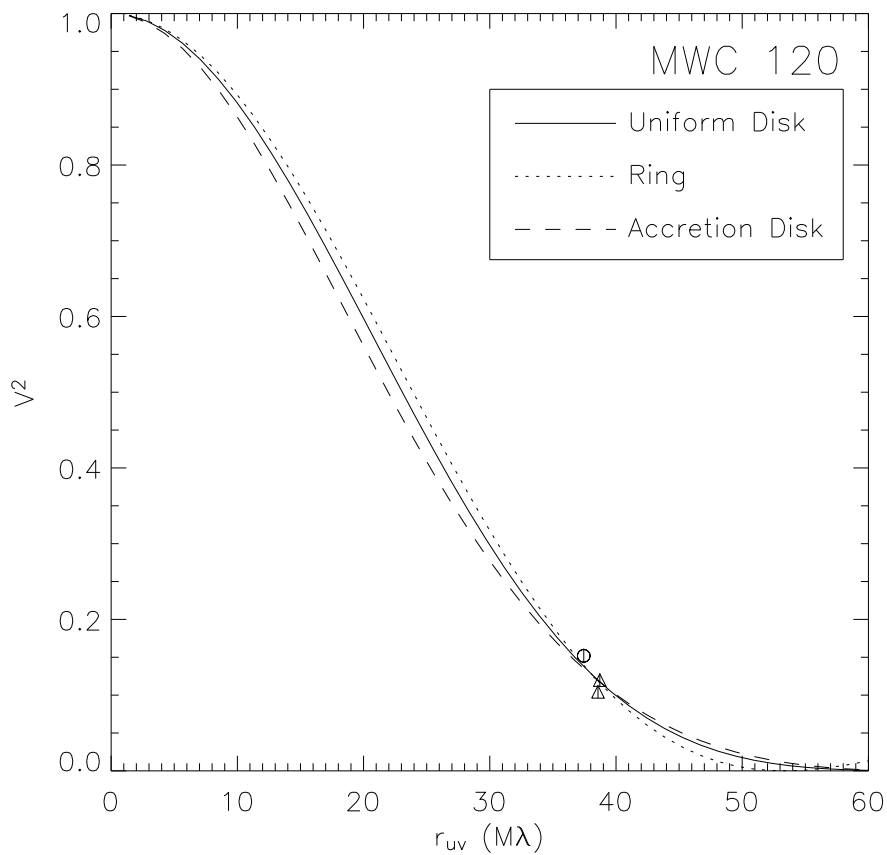


Fig. 7.— V^2 PTI data for MWC 120, as a function of r_{uv} . Symbols and models are plotted as in Figure 2. For this source, the limited $u - v$ coverage does not allow an estimate of inclination, so we plot only face-on models.

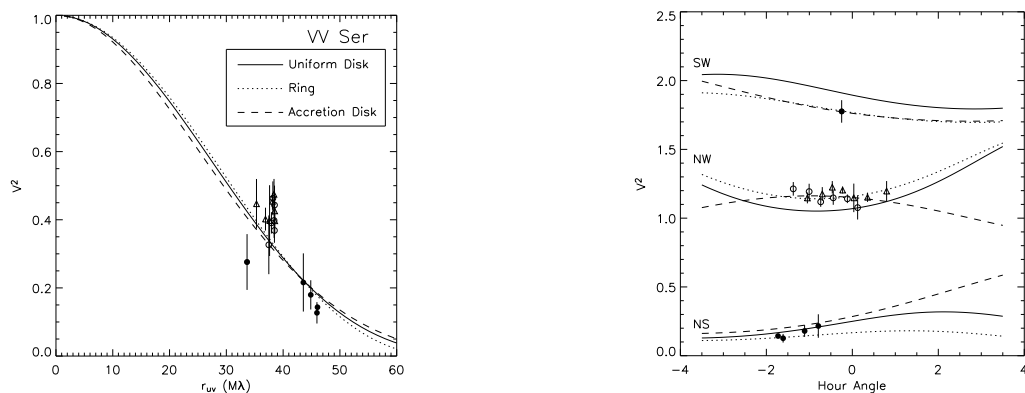


Fig. 8.— V^2 PTI data for VV Ser, as a function of r_{uv} (left panel) and hour angle (right panel). Symbols and models are plotted as in Figure 4. Inclined disk or binary models provide the best fit to the data for this source.

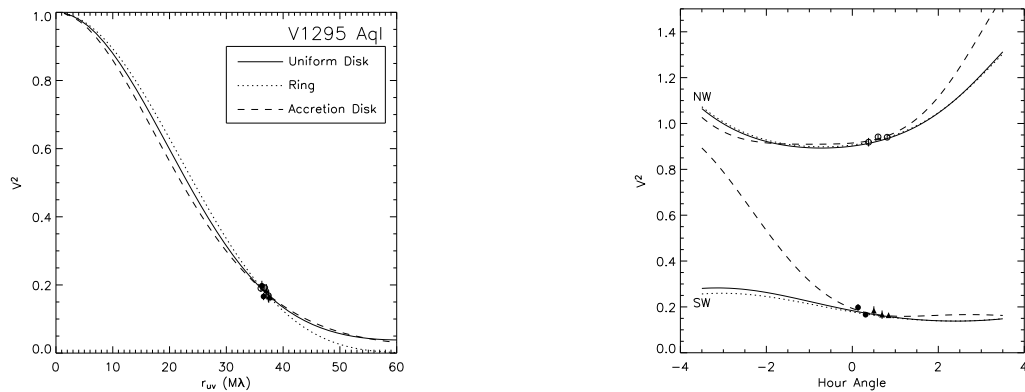


Fig. 9.— V^2 PTI data for V1295 Aql, as a function of r_{uv} (left panel) and hour angle (right panel). Symbols and models are plotted as in Figure 2. For this source, it appears that a face-on disk or a binary model provides the best fit to the data.

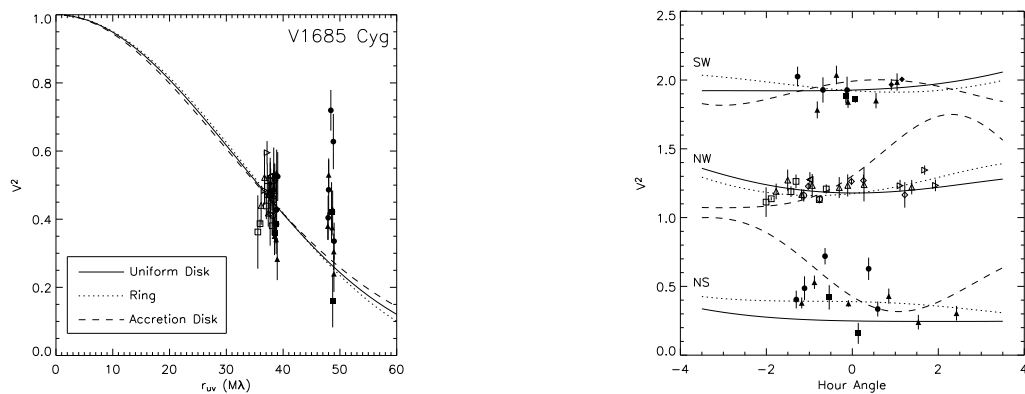


Fig. 10.— V^2 PTI data for V1685 Cyg, as a function of r_{uv} (left panel) and hour angle (right panel). Symbols and models are plotted as in Figure 4. For this source, we see that an inclined disk model provides the best fit to the data, although no models fit all of the data particularly well.

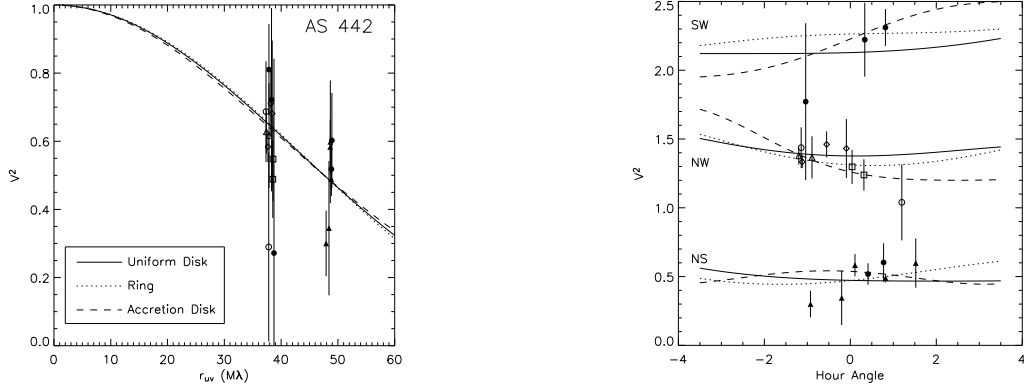


Fig. 11.— V^2 PTI data for AS 442, as a function of r_{uv} (left panel) and hour angle (right panel). Symbols and models are plotted as in Figure 4. Inclined disk or binary models provide the best fit to the data.

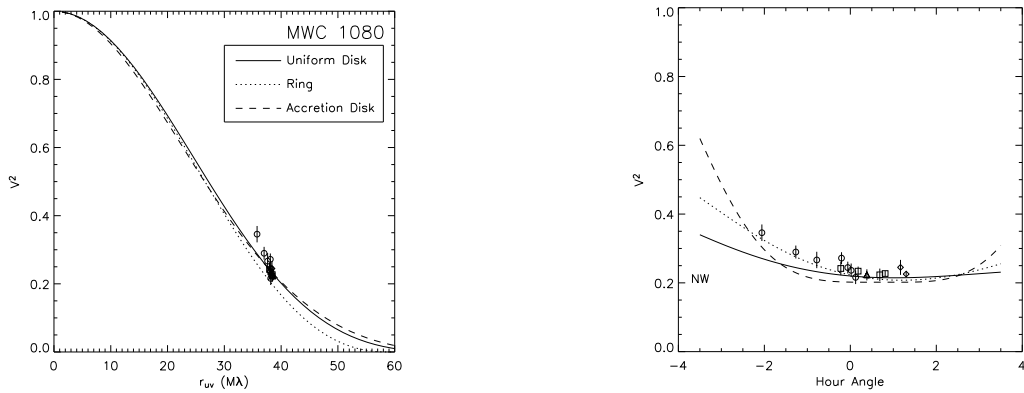


Fig. 12.— V^2 PTI data for MWC 1080, as a function of r_{uv} (left panel) and hour angle (right panel). Symbols and models are plotted as in Figure 2, except that no offset has been applied to the visibilities in the right panel. An inclined disk model provides the best fit to the data.

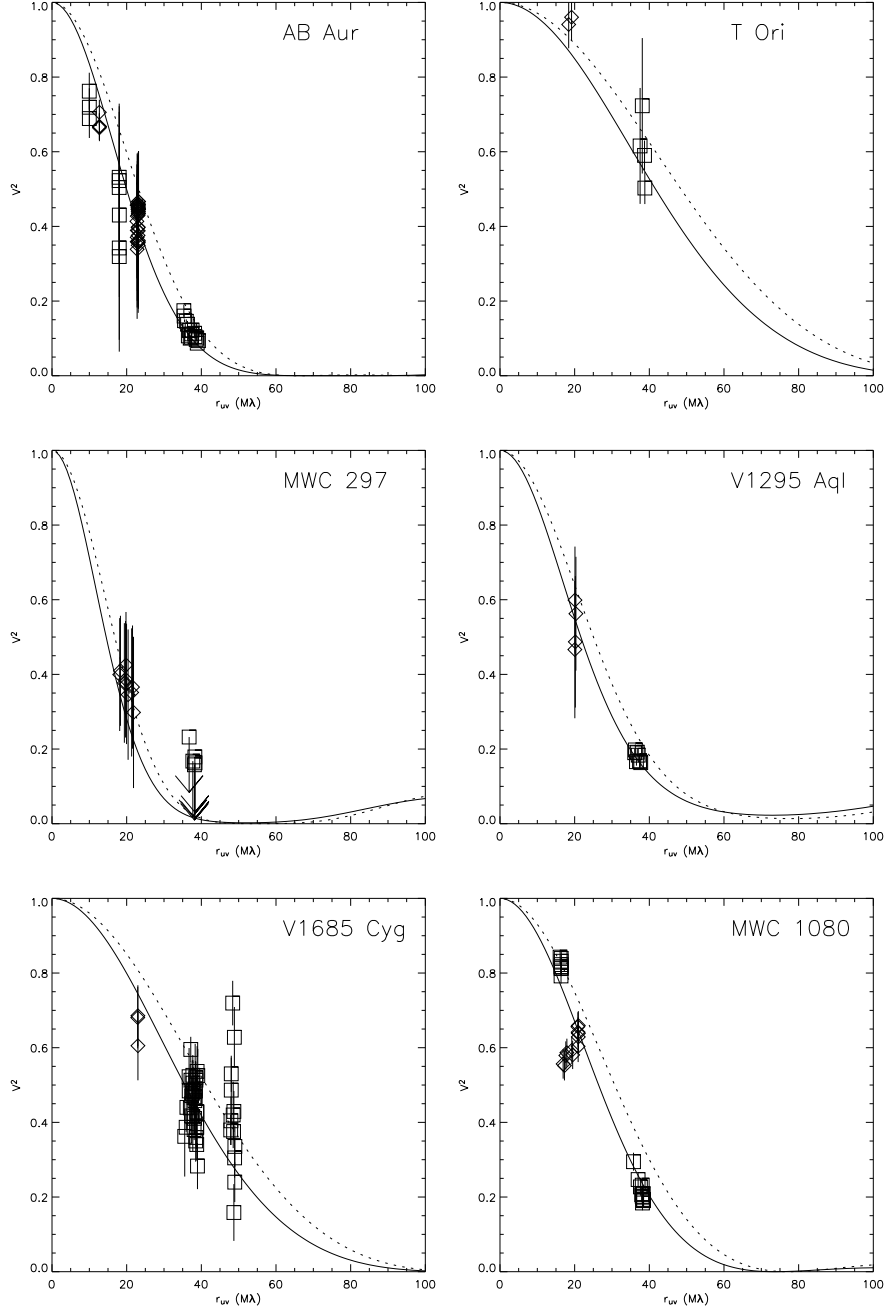


Fig. 13.— PTI and IOTA data for AB Aur, T Ori, MWC 297, V1295 Aql, V1685 Cyg, and MWC 1080, as a function of $r_{uv} = (u^2 + v^2)^{1/2}$. PTI data have $r_{uv} > 30 M\lambda$, and IOTA data have $r_{uv} < 30 M\lambda$. K-band data are represented by squares, and H-band data are plotted with diamonds. The best fit of a face-on flat accretion disk model to the combined dataset is also plotted, where the predicted K-band visibilities are indicated by a solid line and the predicted H-band visibilities are indicated by a dotted line.

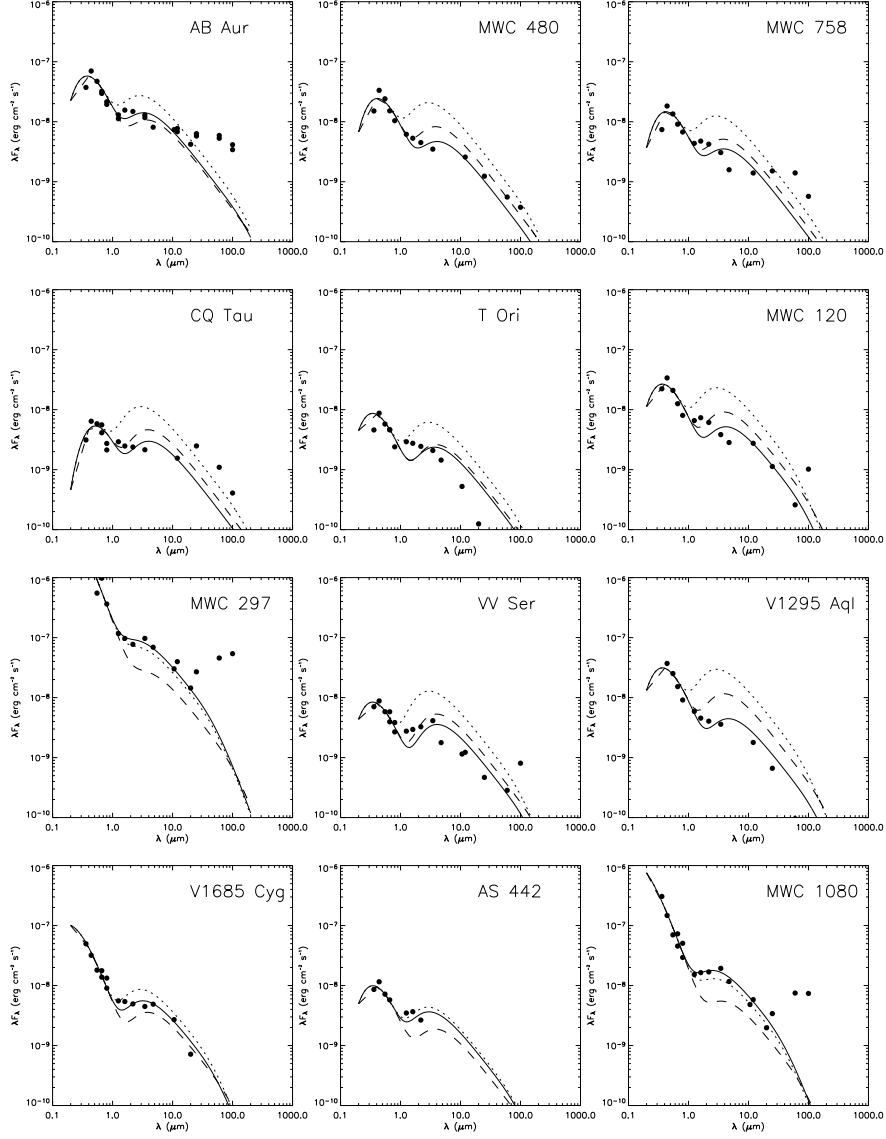


Fig. 14.— Measured SEDs for our sample compiled from the literature and new data (points) and predicted SEDs for geometrically flat accretion disk models (§3.2.2). For each source, we plot the predicted SED for $T_{\text{in}} = 1500$ K (dashed lines), 2000 K (dotted lines), and a value we determined that gives the best fit to the near-IR data (solid lines). The best-fit T_{in} values are listed in Table 11. These models successfully reproduce the SEDs of early-type sources (MWC 297, V1685 Cyg, and MWC 1080), while they are less successful than the flared disk models with puffed-up inner walls (Figure 15) for later-type sources.

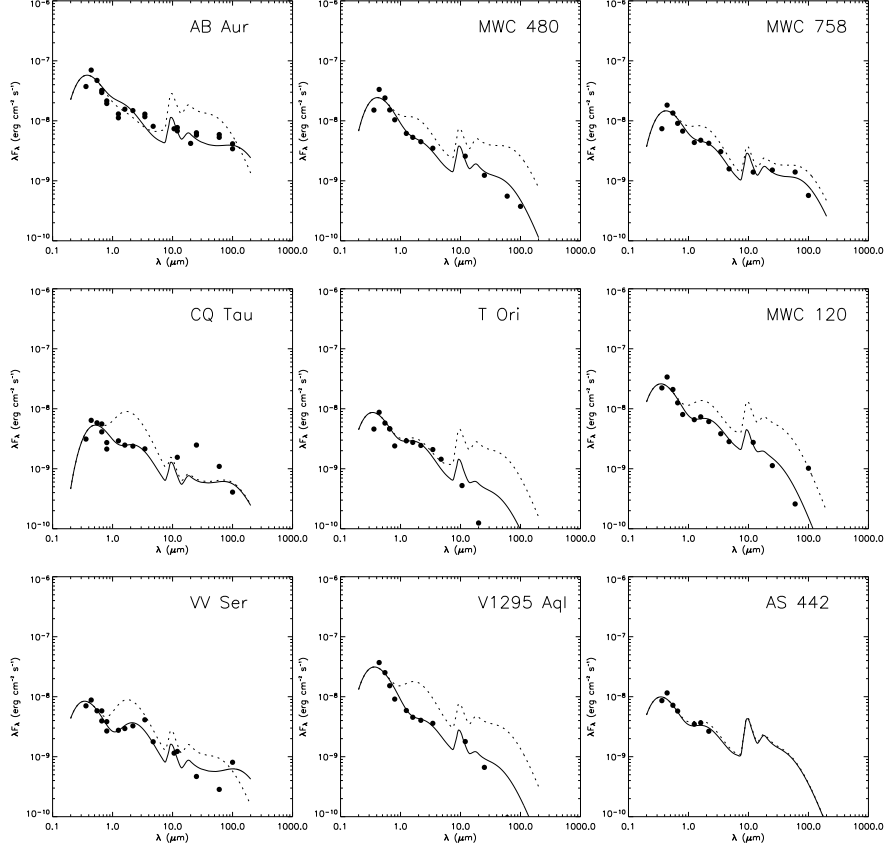


Fig. 15.— Measured SEDs for our sample compiled from the literature and new data (points) and predicted SEDs for flared disk models with puffed-up inner walls (§3.2.3). For each source, we plot the predicted SED for the fiducial model ($T_{\text{in}} = 2000$ K, $\xi = 0.28$, $R_{\text{out}} = 100$ AU; dotted lines) and for a model where the values of T_{in} , ξ , and R_{out} are chosen to give the best fits to the data (solid lines). The best-fit parameter values are listed in Table 11.

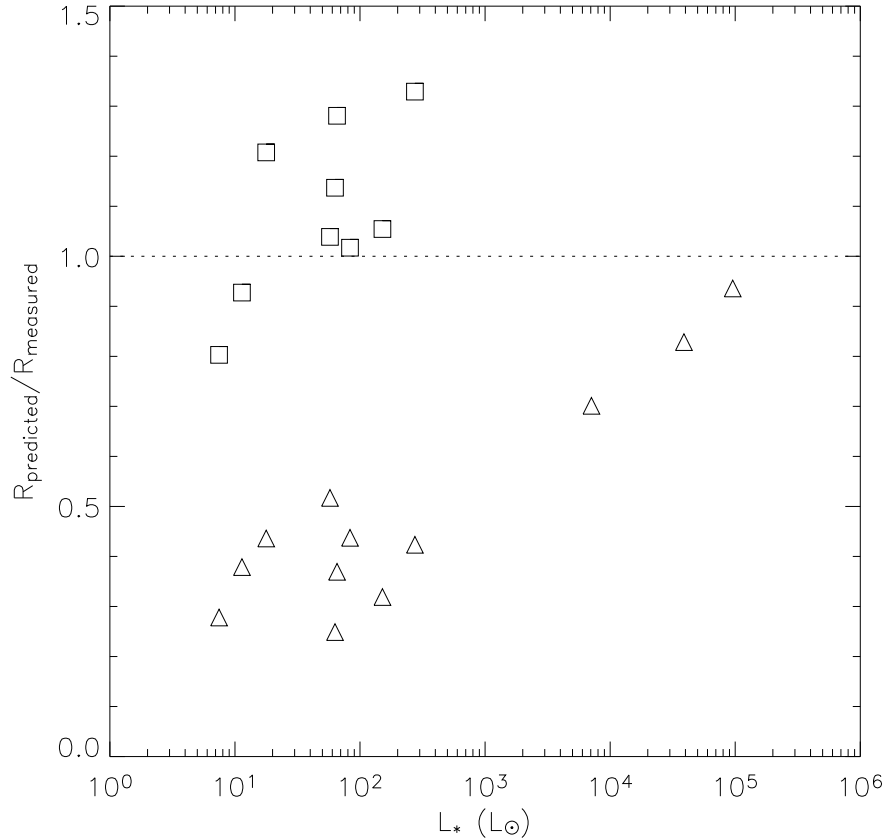


Fig. 16.— The ratio of measured to predicted inner disk sizes, as a function of stellar luminosity. The measured sizes are determined from near-IR interferometry for the geometrically-flat disk model (triangles; §3.2.2) and the puffed-up inner rim model (squares; §3.2.3), and the predicted sizes for each model are computed using the derived stellar parameters to determine the location in the disk where $T = T_{\text{in}}$. The ratio of measured to predicted size is independent of distance (see ELAHS). This figure illustrates that for later-type sources ($L_* < 10^3 L_\odot$), the puffed-up inner disk models predict inner disk sizes within a few tens of percent of the measured sizes, while the flat disk models predict sizes that are off by a factor of ~ 2 . In contrast, the puffed-up inner disk models predict sizes much larger than measured for the early-type objects (not plotted here, since the disagreement is off the scale of the plot), while the flat disk model predicts sizes within $\sim 30\%$ of the measured values.

Table 1. Observed Sources

Source	Alt. Name	α (J2000)	δ (J2000)	d (pc)	Sp.Ty.	V	J	H	K	$F_{K,*}^{\dagger}$ (Jy)	$F_{K,x}^{\dagger}$ (Jy)
AB Aur	HD 31293	04 ^h 55 ^m 45.84 ^s	+30°33′04″.3	140	A0pe	7.1	6.4	5.3	4.5	1.65	9.11
MWC 480	HD 31648	04 ^h 58 ^m 46.27 ^s	+29°50′37″.0	140	A2/3ep+sh	7.7	7.1	6.4	5.7	0.81	2.45
MWC 758	HD 36112	05 ^h 30 ^m 27.53 ^s	+25°19′57″.1	150	A3e	8.3	7.4	6.5	5.8	0.53	2.54
CQ Tau	HD 36910	05 ^h 35 ^m 58.47 ^s	+24°44′54″.1	150	A8V/F2IVea	10.3	8.2	7.4	6.5	0.35	1.38
T Ori	MWC 763	05 ^h 35 ^m 50.40 ^s	−05°28′35″.0	450	A3/5ea	10.6	8.2	7.4	6.5	0.20	1.58
MWC 120	HD 37806	05 ^h 41 ^m 02.29 ^s	−02°43′00″.7	500	B9Ve+sh	7.9	7.0	6.1	5.4	0.53	3.92
HD 141569	SAO 140789	15 ^h 49 ^m 57.75 ^s	−03°55′16″.4	99	B9/A0V	7.1	6.8	6.8	6.7	1.29	0.02
HD 158352	SAO 122418	17 ^h 28 ^m 49.65 ^s	+00°19′50″.3	63	A8V	5.4	5.1	4.9	4.9	8.36	−0.98
MWC 297	NZ Ser	18 ^h 27 ^m 39.60 ^s	−03°49′52″.0	400	O9/B1Ve	12.3	6.0	4.5	3.3	11.65	44.44
VV Ser	HBC 282	18 ^h 28 ^m 47.90 ^s	+00°08′40″.0	310	A0Vep	11.9	8.6	7.5	6.3	0.21	2.16
V1295 Aql	HD 190073	20 ^h 03 ^m 02.51 ^s	+05°44′16″.7	290	B9/A0Vp+sh	7.7	7.1	6.6	5.9	0.85	2.09
V1685 Cyg	BD+40°4124	20 ^h 20 ^m 28.25 ^s	+41°21′51″.6	1000	B2Ve	10.7	7.9	6.8	5.9	0.49	2.91
AS 442	V1977 Cyg	20 ^h 47 ^m 37.47 ^s	+43°47′24″.9	600	B8Ve	11.0	8.2	7.1	6.5	0.30	1.73
MWC 1080	V628 Cas	23 ^h 17 ^m 26.10 ^s	+60°50′43″.0	1000	B0eq	11.7	7.4	6.0	4.8	0.87	9.85

References. — Distances, spectral types and V magnitudes from Hillenbrand et al. (1992), Thé et al. (1994), Mora et al. (2001), Strom et al. (1972), de Lara et al. (1991), Warren & Hesser (1978), and Bigay & Garner (1970). JHK magnitudes from the present work (§2.1). †: De-reddened fluxes at K-band.

Table 2. Summary of Observations

Source	Date (MJD)	Baseline	HA [†]	Calibrators (HD)	
AB Aur	52575	NW	[1.21,1.85]	29645	
	52601	NW	[-1.80,1.24]	29645,32301	
	52602	NW	[-1.95,1.51]	29645,32301	
	52925	NW	[-2.10,1.23]	29645,32301	
	52926	SW	[-2.86,0.83]	29645,32301	
MWC 480	52575	NW	[-1.61,0.34]	29645	
	52601	NW	[-1.05,0.78]	29645,32301	
	52602	NW	[-0.65,0.63]	29645,32301	
	52925	NW	[-1.91,1.41]	29645,32301	
	52926	SW	[-3.16,1.66]	29645,32301	
MWC 758	52575	NW	[-0.54,0.34]	29645	
	52601	NW	[-2.07,1.37]	29645,32301	
	52602	NW	[-1.61,-1.61]	29645,32301	
	52925	NW	[-1.39,1.09]	29645,32301	
	52926	SW	[-3.28,0.51]	29645,32301	
	52977	NW	[-1.40,-1.40]	29645,32301	
	53018	NS	[-0.52,-0.52]	29645,32301	
	53019	NS	[-1.94,1.11]	29645,32301	
	CQ Tau	52926	SW	[-1.19,0.66]	29645,32301
		52934	SW	[-1.87,-0.5]	29645,32301
52977		NW	[-1.69,0.83]	29645,32301	
53017		NW	[-2.13,-1.32]	29645,32301	
53018		NS	[-0.34,-0.34]	29645,32301	
53019		NS	[-1.79,1.16]	29645,32301	
T Ori	52977	NW	[-0.20,0.09]	33608,38858	
	53017	NW	[-1.06,-0.82]	33608,38858	
MWC 120	52977	NW	[0.21,0.21]	33608,38858	
	53017	NW	[-0.70,-0.21]	33608,38858	
HD 141569	52780	NW	[-0.31,0.46]	139137, 147449	
	52781	NW	[-1.01,-1.01]	139137, 147449	
	52787	NW	[-1.22,0.01]	139137, 147449	
HD 158352	52775	NS	[-2.07,-1.38]	164259,161868	
	52781	NW	[0.33,0.33]	164259,161868	
	52788	NW	[-1.37,0.27]	164259,161868	
MWC 297	52798	NW	[-1.91,-0.86]	164259,171834	
	52826	NW	[-1.17,-0.03]	164259,171834	
VV Ser	52490	NW	[-0.72,0.54]	171834	

Table 2—Continued

Source	Date (MJD)	Baseline	HA [†]	Calibrators (HD)
V1295 Aql	52491	NS	[-1.55,-0.74]	171834
	52493	NW	[-1.31,0.20]	171834
	52499	NW	[-0.96,0.84]	164259,171834
	52869	SW	[-0.25,-0.25]	164259,171834
	52799	NW	[-1.28,-0.66]	187293
	52827	NW	[-0.81,-0.42]	187293,193556
	52828	NW	[-1.55,-0.03]	187293,193556
	52925	NW	[0.42,0.85]	187293,193556
V1685 Cyg	52926	SW	[0.19,0.88]	187293,193556
	52418	NW	[-1.10,-1.00]	192640,192985
	52475	NW	[-1.69,1.44]	192640,192985
	52476	NW	[-1.80,-0.48]	192640,192985
	52490	NW	[-0.97,1.70]	192640
	52491	NS	[-1.27,2.38]	192640
	52492	NW	[-0.90,-0.90]	192640
	52545	NS	[-1.12,2.48]	192640,192985
AS 442	52869	SW	[-1.24,0.71]	192640,192985
	52878	SW	[-0.76,1.08]	192640,192985
	52879	SW	[-0.49,0.23]	192640,192985
	52925	NW	[1.14,1.97]	192640,192985
	52926	SW	[0.94,1.19]	192640
	52475	NW	[0.21,1.33]	192640,192985
	52476	NW	[-0.21,-0.21]	192640,192985
	52490	NW	[-1.11,0.38]	192640
MWC 1080	52491	NS	[-0.69,2.54]	192640
	52492	NW	[-1.05,0.00]	192640
	52545	NS	[-0.87,1.58]	192640,192985
	52878	SW	[-0.99,0.86]	192640,192985
	52475	NW	[0.17,0.17]	219623
	52475	NW	[-1.99,0.52]	219623
	52490	NW	[-0.14,1.39]	219623

References. — †: Hour angle coverage of the observations.

Table 3. Properties of Calibrator Sources

Name	α (J2000)	δ (J2000)	Sp.Ty.	V	K	Cal. Size (mas)	$\Delta\alpha$ ($^{\circ}$)
HD 29645	04 ^h 41 ^m 50.26 ^s	+38°16'48''7	G0V	6.0	4.6	0.56 ± 0.04	8.2 ^a , 9.1 ^b , 16.5 ^c , 17.7 ^d
HD 32301	05 ^h 03 ^m 05.75 ^s	+21°35'23''9	A7V	4.6	4.1	0.47 ± 0.11	9.1 ^a , 8.3 ^b , 7.3 ^c , 8.2 ^d
HD 33608	05 ^h 11 ^m 19.18 ^s	−02°29'26''8	F5V	5.9	4.8	0.47 ± 0.05	6.5 ^e , 7.4 ^f
HD 38858	05 ^h 48 ^m 34.94 ^s	−04°05'40''7	G4V	6.0	4.4	0.56 ± 0.01	3.2 ^e , 2.3 ^f
HD 139137	15 ^h 36 ^m 33.71 ^s	−00°33'41''5	G8III	6.5	4.3	0.57 ± 0.08	4.7 ^g
HD 147449	16 ^h 22 ^m 04.35 ^s	+01°01'44''5	F0V	4.8	4.1	0.65 ± 0.04	9.4 ^g
HD 161868	17 ^h 47 ^m 53.56 ^s	+02°42'26''2	A0V	3.8	3.8	0.62 ± 0.12	5.3 ^h
HD 164259	18 ^h 00 ^m 29.01 ^s	−03°41'25''0	F2IV	4.6	3.7	0.77 ± 0.04	8.9 ^h , 7.0 ⁱ , 7.5 ^j
HD 171834	18 ^h 36 ^m 39.08 ^s	+06°40'18''5	F3V	5.4	4.5	0.54 ± 0.06	9.1 ⁱ , 6.8 ^j
HD 187293	19 ^h 52 ^m 03.44 ^s	+11°37'42''0	G0V	6.2	4.8	0.49 ± 0.05	6.5 ^k
HD 193556	20 ^h 20 ^m 20.52 ^s	+14°34'09''3	G8III	6.2	4.0	0.82 ± 0.05	9.8 ^k
HD 192640	20 ^h 14 ^m 32.03 ^s	+36°48'22''7	A2V	4.9	4.9	0.46 ± 0.01	4.7 ^l , 9.4 ^m
HD 192985	20 ^h 16 ^m 00.62 ^s	+45°34'46''3	F5V	5.9	4.8	0.44 ± 0.03	4.3 ^l , 5.9 ^m
HD 219623	23 ^h 16 ^m 42.30 ^s	+53°12'48''5	F7V	5.6	4.3	0.54 ± 0.02	9.5 ⁿ

References. — $\Delta\alpha$ is the offset on the sky between target and calibrator. a: Offset from AB Aur. b: Offset from MWC 480. c: Offset from MWC 758. d: Offset from CQ Tau. e: Offset from T Ori. f: Offset from MWC 120. g: Offset from HD 141569. h: Offset from HD 158352. i: Offset from MWC 297. j: Offset from VV Ser. k: Offset from V1295 Aql. l: Offset from V1685 Cyg. m: Offset from AS 442. n: Offset from MWC 1080.

Table 4. Uniform Disk Models

Source	Face-On Models		Inclined Models			
	χ_r^2	θ (mas)	χ_r^2	θ (mas)	ψ ($^\circ$)	ϕ ($^\circ$)
AB Aur	2.008	$5.31^{+0.01}_{-0.01}$	2.112	$5.34^{+0.06}_{-0.05}$	130^{+50}_{-130}	9^{+6}_{-9}
MWC 480	5.196	$4.85^{+0.01}_{-0.02}$	1.543	$4.99^{+0.07}_{-0.05}$	154^{+16}_{-13}	26^{+4}_{-2}
MWC 758	4.695	$3.69^{+0.02}_{-0.02}$	0.789	$4.15^{+0.10}_{-0.10}$	128^{+3}_{-4}	36^{+2}_{-3}
CQ Tau	5.567	$3.68^{+0.05}_{-0.05}$	0.975	$4.38^{+0.18}_{-0.19}$	105^{+5}_{-5}	48^{+3}_{-5}
T Ori	1.001	$2.71^{+0.11}_{-0.11}$				
MWC 120	2.736	$4.94^{+0.04}_{-0.03}$				
MWC 297		> 5.02				
VV Ser	6.077	$3.68^{+0.03}_{-0.03}$	0.816	$4.49^{+0.87}_{-0.46}$	168^{+22}_{-12}	43^{+10}_{-5}
V1295 Aql	0.623	$5.57^{+0.04}_{-0.04}$	0.716	$5.77^{+0.62}_{-0.27}$	10^{+170}_{-10}	19^{+41}_{-19}
V1685 Cyg	6.805	$3.25^{+0.01}_{-0.02}$	3.905	$3.59^{+0.07}_{-0.06}$	110^{+3}_{-4}	41^{+3}_{-2}
AS 442	1.039	$2.44^{+0.06}_{-0.06}$	0.872	$2.74^{+0.26}_{-0.29}$	58^{+59}_{-11}	47^{+28}_{-33}
MWC 1080	1.251	$4.09^{+0.01}_{-0.02}$	0.466	$4.13^{+0.24}_{-0.05}$	55^{+12}_{-45}	34^{+23}_{-15}

References. — Columns 2-3 contain the reduced chi squared and angular size values for best-fit face-on disk models. Columns 4-7 list χ_r^2 , angular size, position angle, and inclination for best-fit inclined disk models. For T Ori, MWC 120, and MWC 297, we fit only face-on models, and the quoted angular size for MWC 297 is a lower limit.

Table 5. Gaussian Models

Source	Face-On Models		Inclined Models			
	χ_r^2	θ (mas)	χ_r^2	θ (mas)	ψ ($^\circ$)	ϕ ($^\circ$)
AB Aur	4.365	$3.60^{+0.01}_{-0.01}$	3.279	$3.69^{+0.04}_{-0.04}$	157^{+33}_{-157}	16^{+3}_{-3}
MWC 480	5.860	$3.21^{+0.02}_{-0.01}$	1.330	$3.36^{+0.07}_{-0.05}$	149^{+17}_{-9}	32^{+4}_{-4}
MWC 758	2.715	$2.34^{+0.01}_{-0.01}$	0.598	$2.57^{+0.08}_{-0.07}$	130^{+6}_{-5}	33^{+4}_{-4}
CQ Tau	4.470	$2.32^{+0.03}_{-0.04}$	0.871	$2.75^{+0.13}_{-0.13}$	104^{+6}_{-6}	48^{+4}_{-5}
T Ori	1.006	$1.64^{+0.07}_{-0.07}$				
MWC 120	3.576	$3.29^{+0.04}_{-0.03}$				
MWC 297		> 3.35				
VV Ser	7.963	$2.33^{+0.02}_{-0.01}$	0.802	$2.92^{+0.63}_{-0.29}$	173^{+20}_{-16}	47^{+9}_{-4}
V1295 Aql	0.697	$3.85^{+0.04}_{-0.05}$	0.666	$4.29^{+1.20}_{-0.50}$	110^{+70}_{-110}	50^{+30}_{-50}
V1685 Cyg	6.145	$2.00^{+0.02}_{-0.01}$	3.895	$2.21^{+0.05}_{-0.04}$	110^{+4}_{-4}	41^{+3}_{-3}
AS 442	1.000	$1.49^{+0.04}_{-0.04}$	0.868	$1.66^{+0.17}_{-0.18}$	57^{+62}_{-12}	47^{+30}_{-36}
MWC 1080	1.462	$2.59^{+0.01}_{-0.01}$	0.460	$2.62^{+0.16}_{-0.03}$	56^{+10}_{-41}	40^{+25}_{-17}

References. — Columns defined as in Table 4.

Table 6. Ring Models

Source	Face-On Models		Inclined Models			
	χ_r^2	θ (mas)	χ_r^2	θ (mas)	ψ ($^\circ$)	ϕ ($^\circ$)
AB Aur	2.263	$3.23^{+0.01}_{-0.01}$	2.016	$3.25^{+0.03}_{-0.02}$	105^{+75}_{-105}	9^{+5}_{-9}
MWC 480	4.879	$2.97^{+0.01}_{-0.01}$	1.390	$3.05^{+0.03}_{-0.03}$	155^{+17}_{-14}	24^{+3}_{-2}
MWC 758	6.149	$2.31^{+0.01}_{-0.01}$	0.938	$2.62^{+0.05}_{-0.05}$	127^{+3}_{-4}	37^{+2}_{-2}
CQ Tau	6.254	$2.30^{+0.03}_{-0.02}$	1.033	$2.75^{+0.10}_{-0.11}$	106^{+4}_{-5}	48^{+3}_{-4}
T Ori	1.000	$1.73^{+0.06}_{-0.06}$				
MWC 120	2.339	$3.03^{+0.02}_{-0.02}$				
MWC 297		> 2.95				
VV Ser	5.194	$2.30^{+0.01}_{-0.01}$	0.822	$2.80^{+0.50}_{-0.31}$	165^{+13}_{-10}	42^{+10}_{-7}
V1295 Aql	0.647	$3.37^{+0.02}_{-0.01}$	0.748	$3.76^{+0.23}_{-0.42}$	16^{+164}_{-0}	33^{+23}_{-33}
V1685 Cyg	7.198	$1.96^{+0.01}_{-0.01}$	3.914	$2.18^{+0.04}_{-0.04}$	110^{+3}_{-4}	41^{+3}_{-2}
AS 442	1.062	$1.55^{+0.04}_{-0.04}$	0.874	$1.74^{+0.17}_{-0.17}$	59^{+57}_{-9}	46^{+28}_{-30}
MWC 1080	0.706	$2.55^{+0.01}_{-0.01}$	0.344	$2.57^{+0.24}_{-0.02}$	56^{+123}_{-56}	28^{+21}_{-18}

References. — Columns defined as in Table 4.

Table 7. Geometrically Flat Accretion Disk Models

Source	Face-On Models		Inclined Models			
	χ_r^2	θ (mas)	χ_r^2	θ (mas)	ψ ($^\circ$)	ϕ ($^\circ$)
$T_{\text{in}} = 2000$ K						
AB Aur	2.549	$2.24^{+0.01}_{-0.01}$	2.465	$2.26^{+0.03}_{-0.01}$	148^{+32}_{-148}	10^{+6}_{-4}
MWC 480	5.479	$2.03^{+0.01}_{-0.01}$	1.333	$2.10^{+0.03}_{-0.02}$	153^{+15}_{-12}	28^{+5}_{-2}
MWC 758	3.395	$1.51^{+0.01}_{-0.01}$	0.660	$1.69^{+0.03}_{-0.05}$	129^{+5}_{-4}	35^{+3}_{-4}
CQ Tau	4.846	$1.50^{+0.02}_{-0.02}$	0.898	$1.78^{+0.08}_{-0.08}$	105^{+5}_{-6}	48^{+4}_{-5}
T Ori	1.007	$1.08^{+0.04}_{-0.04}$				
MWC 120	3.057	$2.09^{+0.02}_{-0.02}$				
MWC 297		> 2.12				
VV Ser	7.195	$1.52^{+0.01}_{-0.01}$	0.804	$1.86^{+0.40}_{-0.18}$	172^{+20}_{-15}	45^{+10}_{-4}
V1295 Aql	0.631	$2.37^{+0.02}_{-0.01}$	0.694	$2.39^{+0.30}_{-0.05}$	135^{+45}_{-135}	12^{+22}_{-12}
V1685 Cyg	6.330	$1.32^{+0.01}_{-0.01}$	3.896	$1.46^{+0.03}_{-0.03}$	110^{+4}_{-4}	41^{+3}_{-2}
AS 442	1.004	$0.98^{+0.02}_{-0.03}$	0.869	$1.10^{+0.11}_{-0.12}$	57^{+62}_{-12}	48^{+29}_{-35}
MWC 1080	1.372	$1.69^{+0.01}_{-0.01}$	0.461	$1.71^{+0.10}_{-0.02}$	56^{+9}_{-42}	38^{+24}_{-17}
$T_{\text{in}} = 1500$ K						
AB Aur	2.071	$2.49^{+0.01}_{-0.01}$	2.205	$2.50^{+0.03}_{-0.01}$	136^{+44}_{-136}	8^{+7}_{-8}
MWC 480	5.262	$2.27^{+0.01}_{-0.01}$	1.342	$2.34^{+0.03}_{-0.02}$	152^{+18}_{-11}	27^{+4}_{-3}
MWC 758	4.233	$1.71^{+0.01}_{-0.01}$	0.738	$1.93^{+0.04}_{-0.05}$	128^{+4}_{-4}	36^{+2}_{-4}
CQ Tau	5.309	$1.71^{+0.02}_{-0.03}$	0.944	$2.03^{+0.09}_{-0.08}$	105^{+5}_{-5}	48^{+4}_{-5}
T Ori	1.003	$1.25^{+0.05}_{-0.05}$				
MWC 120	2.795	$2.33^{+0.01}_{-0.02}$				
MWC 297		> 2.36				
VV Ser	6.434	$1.72^{+0.01}_{-0.01}$	0.810	$2.11^{+0.42}_{-0.22}$	169^{+22}_{-9}	44^{+10}_{-5}
V1295 Aql	0.623	$2.62^{+0.02}_{-0.01}$	0.712	$2.67^{+0.32}_{-0.08}$	3^{+177}_{-3}	14^{+25}_{-14}
V1685 Cyg	6.631	$1.51^{+0.01}_{-0.01}$	3.903	$1.67^{+0.04}_{-0.02}$	110^{+3}_{-4}	41^{+3}_{-2}
AS 442	1.024	$1.13^{+0.03}_{-0.03}$	0.871	$1.26^{+0.13}_{-0.13}$	58^{+60}_{-8}	46^{+18}_{-33}
MWC 1080	1.300	$1.92^{+0.01}_{-0.01}$	0.471	$1.94^{+0.0}_{-0.02}$	54^{+13}_{-43}	35^{+19}_{-16}

References. — Columns defined as in Table 4.

Table 8. Flared Disk Models with Puffed-Up Inner Walls

Source	Face-On Models		Inclined Models			
	χ_r^2	θ (mas)	χ_r^2	θ (mas)	ψ ($^\circ$)	ϕ ($^\circ$)
$T_{\text{in}} = 2000$ K						
AB Aur	1.994	$3.35^{+0.01}_{-0.01}$	2.163	$3.37^{+0.05}_{-0.03}$	130^{+50}_{-130}	8^{+7}_{-8}
MWC 480	4.919	$3.22^{+0.01}_{-0.01}$	1.387	$3.31^{+0.03}_{-0.03}$	156^{+16}_{-15}	24^{+4}_{-2}
MWC 758	5.858	$2.49^{+0.01}_{-0.01}$	0.921	$2.85^{+0.06}_{-0.05}$	127^{+3}_{-4}	37^{+2}_{-2}
CQ Tau	6.254	$2.51^{+0.04}_{-0.03}$	1.034	$3.01^{+0.10}_{-0.13}$	106^{+4}_{-5}	48^{+3}_{-4}
T Ori	1.006	$1.78^{+0.09}_{-0.10}$				
MWC 120	2.340	$3.31^{+0.02}_{-0.02}$				
VV Ser	5.287	$2.50^{+0.01}_{-0.02}$	0.820	$3.05^{+0.31}_{-0.21}$	165^{+15}_{-5}	42^{+6}_{-2}
V1295 Aql	0.646	$3.67^{+0.02}_{-0.02}$	0.765	$3.84^{+0.47}_{-0.20}$	14^{+166}_{-14}	21^{+19}_{-21}
AS 442	0.990	$1.57^{+0.06}_{-0.07}$	0.871	$1.83^{+0.19}_{-0.27}$	57^{+59}_{-11}	48^{+24}_{-38}
$T_{\text{in}} = 1500$ K						
AB Aur	4.320	$3.13^{+0.01}_{-0.01}$	3.404	$3.15^{+0.06}_{-0.01}$	155^{+25}_{-155}	16^{+3}_{-3}
MWC 480	5.052	$3.16^{+0.01}_{-0.02}$	1.474	$3.27^{+0.03}_{-0.02}$	145^{+9}_{-6}	28^{+2}_{-1}
MWC 758	5.033	$2.42^{+0.01}_{-0.02}$	0.867	$2.78^{+0.08}_{-0.06}$	127^{+4}_{-3}	36^{+3}_{-2}
CQ Tau	6.211	$2.50^{+0.04}_{-0.03}$	1.032	$3.00^{+0.11}_{-0.12}$	106^{+4}_{-5}	48^{+3}_{-4}
T Ori	2.246	$1.41^{+0.23}_{-0.07}$				
MWC 120	2.348	$3.30^{+0.02}_{-0.02}$				
VV Ser	5.585	$2.47^{+0.01}_{-0.02}$	0.818	$3.02^{+0.32}_{-0.24}$	166^{+17}_{-6}	42^{+6}_{-2}
V1295 Aql	0.643	$3.65^{+0.02}_{-0.02}$	0.751	$3.85^{+0.38}_{-0.24}$	14^{+166}_{-14}	23^{+15}_{-23}
AS 442	1.628	$1.36^{+0.02}_{-0.05}$	0.863	$1.49^{+0.32}_{-0.31}$	53^{+58}_{-11}	58^{+16}_{-40}

References. — Columns defined as in Table 4. MWC 297, V1685 Cyg, and MWC 1080 are excluded from this table because the puffed-up inner disk wall model cannot fit the data for these sources.

Table 9. Binary Models

Source	χ_r^2	θ (mas)	ψ ($^\circ$)	R
AB Aur	117.08	$4.06^{+0.01}_{-0.01}$	28^{+1}_{-1}	$0.71^{+0.01}_{-0.01}$
MWC 480	13.46	$3.24^{+0.03}_{-0.03}$	127^{+1}_{-1}	$0.43^{+0.01}_{-0.01}$
MWC 758	14.50	$2.69^{+0.02}_{-0.03}$	26^{+1}_{-1}	$0.48^{+0.01}_{-0.02}$
CQ Tau	4.408	$2.95^{+0.05}_{-0.06}$	32^{+1}_{-1}	$0.48^{+0.03}_{-0.04}$
VV Ser	0.750	$9.27^{+3.44}_{-2.74}$	175^{+1}_{-172}	$0.55^{+0.16}_{-0.03}$
V1295 Aql	0.692	$3.09^{+2.52}_{-0.20}$	109^{+25}_{-102}	$0.43^{+0.33}_{-0.02}$
V1685 Cyg	14.90	$3.61^{+0.04}_{-0.05}$	135^{+1}_{-1}	$0.28^{+0.01}_{-0.01}$
AS 442	0.864	$2.69^{+0.21}_{-0.69}$	30^{+19}_{-8}	$0.20^{+0.07}_{-0.01}$
MWC 1080	0.774	$2.55^{+0.11}_{-0.31}$	63^{+5}_{-5}	$0.38^{+0.05}_{-0.01}$

References. — Columns 2-5 list the reduced chi squared values, angular separations, position angles, and brightness ratios of best-fit binary models. T Ori, MWC 120, and MWC 297 are excluded from this table because the limited $u - v$ coverage for these sources is insufficient to constrain the parameters of the model.

Table 10. Accretion Disk Models for PTI+IOTA Visibilities

Source	Face-On Models		Inclined Models			
	χ_r^2	θ (mas)	χ_r^2	θ (mas)	ψ ($^\circ$)	ϕ ($^\circ$)
$T_{\text{in}} = 2000$ K						
AB Aur	2.495	$2.26^{+0.01}_{-0.01}$	2.889	$2.27^{+0.02}_{-0.01}$	170^{+0}_{-170}	11^{+4}_{-3}
T Ori	0.834	$1.08^{+0.04}_{-0.05}$				
MWC 297	0.040	$3.38^{+0.24}_{-0.22}$				
V1295 Aql	0.604	$2.38^{+0.02}_{-0.02}$	0.343	$2.68^{+0.11}_{-0.33}$	15^{+165}_{-15}	35^{+4}_{-35}
V1685 Cyg	6.141	$1.32^{+0.01}_{-0.01}$	2.021	$1.46^{+0.03}_{-0.02}$	111^{+3}_{-4}	41^{+3}_{-3}
MWC 1080	9.355	$1.69^{+0.01}_{-0.01}$	6.408	$1.76^{+0.03}_{-0.03}$	43^{+6}_{-4}	37^{+5}_{-5}

References. — Columns defined as in Table 4.

Table 11. Disk Parameters from Near-IR Interferometry and SEDs

Source	Flat Disks		Flared, Puffed-Up Inner Disks			
	R_{in} (AU)	T_{in} (K)	R_{in} (AU)	T_{in} (K)	ξ	R_{out} (AU)
AB Aur	0.17	1690	0.25	2230	0.12	360
MWC 480	0.16	1370	0.23	1580	0.16	30
MWC 758	0.14	1450	0.21	1700	0.24	70
CQ Tau	0.15	1430	0.23	1470	0.28	100
T Ori	0.28	1570	0.40	1950	0.10	30
MWC 120	0.58	1370	0.83	1690	0.14	30
MWC 297	0.68	2140				
VV Ser	0.33	1450	0.47	1630	0.20	400
V1295 Aql	0.39	1240	0.55	1390	0.12	30
V1685 Cyg	0.73	1790				
AS 442	0.33	1910	0.55	1910	0.28	100
MWC 1080	0.86	2170				

References. — Columns 2-3 list the inner disk radii and temperatures for geometrically flat disk models (§3.2.2) determined from near-IR interferometry and SEDs. Inner radii are computed from inner disk angular sizes (Table 7, and Table 10 for MWC 297), using the distances assumed in Table 1. Columns 4-7 list the inner radii, inner disk temperatures, flaring indexes, and outer radii determined for flared disk models with puffed-up inner walls (§3.2.3). The inner radii are computed from angular sizes in Table 8 and distances listed in Table 1. Puffed-up inner disk wall models are ruled out for MWC 297, V1685 Cyg, and MWC 1080, and thus no parameter values are listed.